Methane retrieval retrievals from airborne HySpex observations in the short-wave infrared

Philipp Hochstaffl[1], Franz Schreier[1], Claas Henning Köhler[1], Andreas Baumgartner[1], and Daniele Cerra[1]

[1]Deutsches Zentrum für Luft- und Raumfahrt, Institut für Methodik der Fernerkundung, 82234 Oberpfaffenhofen, Germany

Correspondence: Philipp Hochstaffl (philipp.hochstaffl@dlr.de)

Abstract. A reduction of methane emissions could help to mitigate global warming on a short time scale, making monitoring of local and regional anthropogenic methane emissions crucial for so monitoring anthropogenic emissions is critical to understanding the methane budget . The and its impact on climate. This study compares various retrieval schemes for estimating localized methane enhancements around ventilation shafts in the Upper Silesian Coal Basin in Poland , using nadir observations in the short-wave infrared acquired from the airborne imaging spectrometer HySpex. Nonlinear and linear methods are examined and put into perspective, with an emphasis on strategies to address Linear and nonlinear solvers are examined with special emphasize put on strategies that tackle degeneracies between the surface reflectivity and the broad band molecular absorption features attributed to features—a challenge arising from the instrument's low spectral resolution. The results demonstrate that the weighted Results reveal that the generalized nonlinear least squares fitin , employed within the Beer InfraRed Retrieval Algorithm (BIRRA), where can measure enhanced methane levels with notable accuracy and precision. This is accomplished by allowing the scene's background covariance structure accounts for the reflectivity statistics, is able to quantify enhanced methane levels from hyperspectral data with good accuracy and precision. Some BIRRA setups suffer from surface-type dependent biases although combining multiple spectral intervals mitigates the adverse impact. to account for surface reflectivity statistics. Linear estimators such as the Matched Filter (MF) and the Singular Value Decomposition (SVD) are fast and able to detect andto a certain extend , under favorable conditions, quantify enhanced levels of methane quickly. Using k-means clustering in as a preprocessing step can further enhance the performance of the two linear solvers. The linearized BIRRA fit (LLS) underestimates methane but agrees well on the enhancement pattern. The non-quantitative Spectral Signature Detection (SSD) method does not require any forward modeling and can be useful in the detection of relevant scenes. In conclusion, the BIRRA code— , originally designed for the retrieval of atmospheric constituents from space borne high resolution spectra, turned out to be applicable to hyperspectral airborne imaging data for the quantification of methane plumes from point-like sources. Moreover, it is able to outperform well established linear schemes such as the MF or SVD , however, at the expense of high(er) computing time.

1 Introduction

Methane (CH_4) is the second most important anthropogenic greenhouse gas next to carbon dioxide (CO_2), according to the latest IPCC IPCC (Intergovernmental Panel on Climate Change) report (Masson-Delmotte et al., 2021). Due to its comparatively short lifetime of approximately 9 nine years, a reduction of methane emissions could help to mitigate global warming on a relatively short time scaleof approximately one decade. Despite improvements in monitoring regional and global CH_4 emissions in recent

years, the IPCC report points out that fundamental uncertainties pertaining to the methane budget remain (Intergovernmental Panel on Climate Change, 2014).

Observations indicate an increasing trend in atmospheric content since 2007, the cause of which is still subject to scientific debate. The vast majority of anthropogenic CH_4 emissions is caused by small scale ~~phenomena~~ processes such as agriculture (enteric fermentation & manure),

30 waste management (landfills) and fossil fuel exploitation, where the ~~latter~~ last is responsible for 20-30 % of all anthropogenic CH_4 emissions. Consequently there ~~exists the~~ is a need for continuous long-term methane observations on ~~a global scale~~ local to global scales, in order to foster understanding on the global methane cycle, devise future reduction measures and monitor their effectiveness. The monitoring of anthropogenic emissions of CH_4 and CO_2 is also part of the United Nations Framework Convention on Climate (2015), as nationally determined contributions should be assessed via global stock takes on a ~~5~~ five year

35 basis from 2023 (Article 13 & 14 of the Paris Agreement).

Satellite observations are typically ~~the method of choice for such~~ used for continuous and global long-term ~~observations although~~ monitoring atmospheric composition but also ground based networks such as the Global Atmosphere Watch (GAW) Programme of the World Meteorological Organisation (WMO) or the European Integrated Carbon Observation System (ICOS) are crucial assets~~in monitoring atmospheric composition. Space-borne~~ . Space borne spectrometers measuring short-wave infrared (SWIR) solar radiation

40 reflected at the Earth surface are especially well-suited to observe atmospheric CH_4 in the lower atmosphere by measuring its absorption around 1.6 μm and and 2.3 μm. In contrast, the thermal infrared is less sensitive to variations in CH_4 concentration close to the surface. Moreover, mid-infrared sensors often have lower spatial resolution making them less favorable for emission monitoring (Richter, 2010).

Operational CH_4 products from contemporary atmospheric composition missions such as TROPOMI (TROPOspheric Mon-

45 itoring Instrument; ~~Veefkind et al. (2012)~~ Veefkind et al. 2012), GOSAT/GOSAT-2 (Greenhouse gases Observing SATellite; ~~Kuze et al. (2009, 2016)~~ Kuze et al. 2009, 2016) measure trace gas concentrations with very high accuracy~~, nevertheless,~~ . Nevertheless, they are not optimally suited to measure emissions of ~~point-like~~ point sources. This ~~design~~ inherent limitation is due to their focus on rapid global coverage, which entails a comparatively coarse spatial resolution of several square kilometers per pixel. Since the emission of a single point source inside a pixel is averaged over the entire resolution cell, even large sources seldomly elevate

50 the mean CH_4 concentration within one pixel by more than one percent compared to the undisturbed background (Lauvaux et al., 2022). A way to increase the contrast of enhancements is to operate typical atmospheric remote sensing spectrometers at lower altitudes (e.g. on aircraft), thus increasing the spatial resolution while leaving the overall optical design untouched. This strategy is followed by instruments such as MAMAP/MAMAP-2D (Gerilowski et al., 2011) or GHOST (Humpage et al., 2018) which are ~~very~~ well-suited for the calibration and validation of their ~~space-borne~~ space borne counterparts.

55 In order to increase the sensitivity towards smaller sources an increased spatial resolution is required. This in turn necessitates a trade-off in spectral resolution because the loss of photons caused by the smaller ground pixels reduces the Signal-to-Noise Ratio (SNR) of the image, which has to be compensated by broadening the ~~spectral interval per spectral channel~~ width of the spectral channels. Imaging spectrometers for land surface remote sensing (often referred to as hyperspectral cameras) are typical examples of instruments optimized for spatial resolution this way. Their technology matured over the last 30 years and a

60 variety of airborne instruments and several ~~space-borne~~ space borne versions are either in orbit Guanter et al. (2021, PRISMA), Chabrillat et al.

(2020, ENMAP) (Cogliati et al., 2021, PRISMA), (Guanter et al., 2015; Chabrillat et al., 2020, ENMAP) or going to be launched in the future Rast et al. (2021, CHIME)(Rast et al., 2021, CHIME). Yet other sensors dedicated for the detection of methane Jervis et al. (2021, GHGSat) or MethaneSat and or carbon dioxide, e. g., Hochstaffl et al. (2023, CO2Image), GHGSat (Jervis et al., 2021), CO2Image (Hochstaffl et al., 2023) or MethaneSat, have slightly higher spectral resolution than their hyperspectral counterparts but still offer a much higher spatial resolution than atmospheric composition missions.

Thorpe et al. (2013) were the first to demonstrate that localized CH_4 emissions over land can be detected from hyperspectral cameras with the Airborne Visible/Infrared Imaging Spectrometer Green et al. (1998, AVIRIS) (Green et al., 1998, AVIRIS) and that a limited quantitative analysis is possible (Thorpe et al., 2014). Similar studies were repeated with airborne instruments (AVIRIS-NG, Frankenberg et al. 2016; Duren et al. 2019; Borchardt et al. 2021; HySpex, Nesme et al. 2020) and space-borne space borne instruments (Thompson et al., 2016; Guanter et al., 2021). Varon et al. (2019) and Jervis et al. (2021) demonstrated that CH_4 sources can even be detected with the multi-spectral MSI instrument on-board the Sentinel-2 satellites, but these measurements are restricted to 'favourable conditions' (i. e., strong sources and high surface albedo).

One of the core challenges when retrieving methane from measurements with high spatial ($\approx$ <100 m) and moderate spectral resolution ($> 1 \approx$ >1 nm) is the separation of spectral variations caused by molecular absorption and surface reflectivity (Ayasse et al., 2018). Classical methods for trace gas retrievals for from high-spectral resolution instruments such as RemoteC (Lorente et al., 2021), Weighting Function Modified Differential Optical Absorption Spectroscopy (Buchwitz et al., 2005, WFM-DOAS), or the Beer InfraRed Retrieval Algorithm (Gimeno García et al., 2011, BIRRA) exploit the high frequency characteristics of gaseous absorption and attribute the smooth varying part to the surface albedo and scattering. Instruments with coarse spectral resolution, however, are unable to sufficiently resolve those molecular signatures which causes ambiguities that often leads lead to surface-type related biases in the 'classical' 'classical' retrieval schemes (e. g., Borchardt et al. (2021, Sec. 3.3) or Thorpe et al. (2014, Sec. 9.2)). Alternative more 'data-driven' 'data-driven' retrieval schemes such as the Matched Filter (MF) or the Singular Value Decomposition (SVD) estimate enhancements based on methods from linear algebra and statistics (Thorpe et al., 2013; Thompson et al., 2015; Thorpe et al., 2014).

This study aims to compare various retrieval schemes applied to measurements from concentration enhancements from measurements of the German Aerospace Center's (DLR) HySpex sensor system . The objective is to evaluate the retrievals performance in terms of accuracy, precision and speed and show advantages and drawbacks for each method. Another goal is to assess the latest BIRRA updates and its applicability to moderately resolved spectra from airborne sensors. Therefore, the paper is structured as follows: . First, the experimental setup is briefly described, followed by a quick review of atmospheric radiation and an introduction to the various BIRRA setups examined in this study. AfterwardAfterwards, other simpler but faster retrieval schemes employed in this work are briefly discussed. The result section starts with a feasibility analysis and then proceeds with the presentation of the retrieval results from HySpex observations over the Pniowek V ventilation shafts. In the last section, the results are summarized and put into perspective.

2 Methodology

The methodology introduced in this section can be divided into Both linear and nonlinear schemes retrieval schemes for methane enhancements

95   are examined. While the former are very fast and often of but often lack sufficient accuracy, the nonlinear iterative solvers require

more computing power and time to come up with a best estimate. The retrieval methods are tailored to address the issue of albedo-related biases, which

arises due to correlations with broad-band absorption features resulting from the instrument's low spectral resolution.

The data analyzed in this study was collected with the DLR study utilizes measurements collected by the DLR airborne HySpex sensor

system during a survey flight conducted (see Table 1) within the scope of the COMET (Carbon diOxide and METhane) campaign on

100   June 7th, 2018. The CoMet campaign 2018 that focused on the detection and characterization of CO_2 and CH_4 sources in the Upper

Silesian Coal Basin (USCB) in southern Poland.
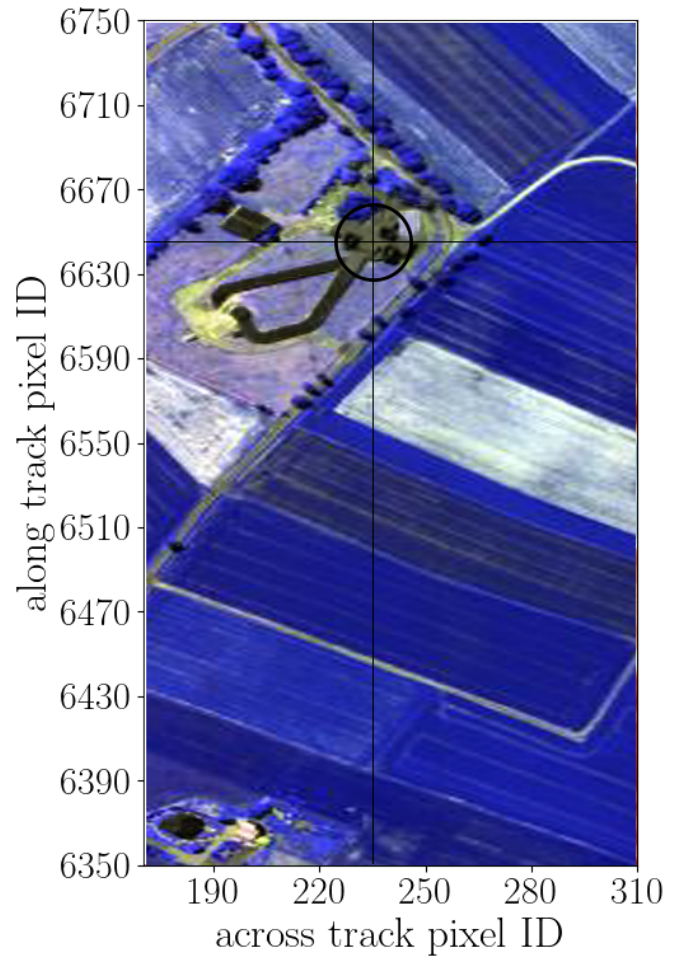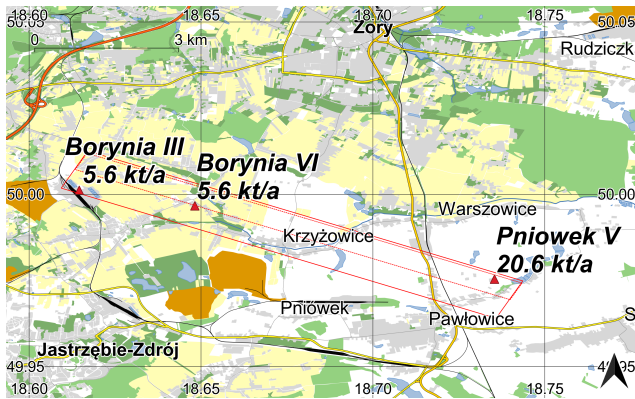
Figure 1. **(a)** **(Left, Top)** Flight lines 09 and 11 are illustrated as a dashed red line and a solid red line, respectively. Flight line 9 (dashed redline) was obtained around 09:55 UTC, while Flight line 11 (solid redline) was acquired around 10:10 UTC (OpenStreetMap contributors, 2022). The aircraft flew at an altitude of approximately $\approx 1.200 \approx 1\,200$ m and $\approx 2.600 \approx 2\,600$ m above ground level, respectively, while heading eastward at 115 degrees. The map was generated using QGIS software and OpenStreetMap data (OpenStreetMap contributors, 2022) **(Left, Bottom)** Photograph of the ventilation shafts from the Pniowek V site. **(b)** Photo credit: Leon Scheidweiler (Uni Heidelberg). **(Right)** False color image from the SWIR-320m-e camera around the three Pniovek V shafts in scene 09.

The airborne imaging spectrometer HySpex consists of two commercially available hyperspectral cameras (a VNIR-1600 and a SWIR-320m-e) and its basic specifications are presented in Table 1. The aim of this survey was to conduct evaluate the feasibility of localized methane emission retrieval using the SWIR-320m-e data. To achieve this goal we planned 18 flight lines at two different altitudes over a number of known ventilation shafts around Katowice. However, it was not known in advance which of these ventilation shafts would be actively emitting methane during overpass, because only monthly averages of the emission rates are reported by the mining companies operating the shafts Nickl et al. (2020) To compare the performance of various retrieval methods, we limit our analysis to the two flight lines shown in Fig. 1,

namely Flight line 9 (called scene 09) and Flight line 11 (called scene 11). The weather during the survey was well-suited for remote sensing measurements. Apart from very few occasional patches of thin cirrus clouds there were no further low or mid-level clouds. Actual wind data for the USCB area is presented in Luther et al. (2022, Fig. 4 and 6).

Table 1. Summary of some important HySpex properties. The sensor is described in detail in (IMF) C. H. Köhler (2016) and references therein.

HySpex specifications	
Detector	MCT Sofradir MARS
Spectral Range [nm]	968-2498
Field of View (with FoV Expander) [°]	13.2 / 27.2
Number of (spectral) Channels	256
Sampling Interval [nm]	6.0
Bandwidth [nm]	5.6–7.0
Number of (geometric) Pixels	320
Dynamic Range [bit]	14

110   The weather during the survey was well-suited for remote sensing measurements. Apart from very few occasional patches of thin cirrus clouds there were no further low or mid-infrared-level clouds. However, some amount of haze was observed from the aircraft during the flights. Actual wind data for the USCB area on the measurement day is presented in Luther et al. (2022, Fig. 4 and 6). Fig. 1 displays the flight tracks over the Pniovek V and other two shafts. It took the aircraft approximately three minutes to complete one track, during which time 7130 (scene 09) and 5075 (scene 11) observations were recorded for each of the 320 across-track detector pixels. To compare the effectiveness of various retrieval methods, we limit our analysis to the two flight lines shown in Fig. **??**, namely Flight line 9 (called scene 09) and Flight line 11 (called scene 11). The map also depicts the location

115 of the potential sources with their nominal (reported) emission rates.

    In Fig. Figure **??** 2 (top) displays an ensemble of along track averaged HySpex measurements is depicted. The sensor's sampling distance across the spectral axis is indicated by the vertical grid lines observations. A possible bad pixel (number 104) is shown in the right plot around 1.65 nm (a descending cyan line). The spectral coverage of the HySpex SWIR-320m-e camera ranges from 967–2496 nm (4005–10338 cm^{-1}), with the exact number depending on the across track pixel detector ($\approx \pm 1$ cm^{-1}). The figure shows that the radiative intensity

120 in the interval around 1.6 μm (≈ 6000 cm^{-1}) is significantly larger than that between 2.3 μm (≈ 4300 cm^{-1}) mostly due to absorption.

    The values for the spectral resolution, i. e., the full width at half maximum (FWHM) of the SWIR-320m-e camera in the 1500–2500 nm (4000–6500 cm^{-1}) region ranges from 6.0–9.5 nm (10–40 cm^{-1}), are provided for each across track pixel of the detector (a 2D array) and is provided with the level 1b data set. This data set was basically created as described in Lenhard et al. (2015), except for the optical distortion correction. The Instrument Spectral Response Function (ISRF) calibration was performed according to Baumgartner (2021). Hence, the ISRF for each pixel is available as a lookup table with an for a sampling

125 distance of 1.2 nm. The figure shows that the radiative intensity in the interval around 1.6 μm (≈ 6000 cm^{-1}) is significantly larger than the one around 2.3 μm (≈ 4300 cm^{-1}) mostly due to H_2O absorption (see Fig. 3). Also the surface reflectivity, depicted in Fig. 1, causes spectral variations in the observed radiance.

2.1 Radiative transfer

In the SWIR spectral range the radiative transfer through the atmosphere under clear sky conditions (cloud and scattering free in general) is well described by Beer's law (Zdunkowski et al., 2007) with the monochromatic transmission in wavenumbers ν given by

$$\mathcal{T}_m(\nu;s) \,=\, \exp\left(-\sum_m \tau_m(\nu,s)\right) \,=\, \exp\left(-\int_{\text{path}} \mathrm{d}s \sum_m n_m(s)\, k_m\big(\nu, p(s), T(s)\big)\right). \tag{1}$$

The model assumes a pure gas atmosphere with molecular of molecules m optical depth τ given , i.e. CH_4, CO_2, H_2O. Optical depth τ_m is calculated by the path integral along s over the molecular number densities n_m and k_m, the pressure p and temperature T dependent absorption cross section . This k_m. The study utilizes the 2020 spectroscopic line data from GEISA (Gestion et Etude des Informations Spectroscopiques Atmosph'eriques Atmosphériques; Delahaye et al., 2021) for molecular absorption calculations.

Figure 2. (a) **(Left)** HySpex average spectrum with the span (minimum to maximum) depicted in gray for measurements across the 320 across track detector pixels detectors for scene 09 (left). The center shows 09. **(Middle)** Shows a bunch of individual spectra around 1.67 μm with the black lines indicating the pixel positions and sampling distance. The radiance values of pixel 104 (cyan) at ≈ 1.677 μm (5960 cm^{-1}), which is relevant for the CH4 retrieval, appears to be problematic. (b) **(Right)** Reference reflectances for different surface types (measured at the John Hopkins University Baldridge et al. 2009; Meerdink et al. 2019).

 The decision to exclude aerosol modelling for HySpex observations was encouraged by findings from Borchardt et al. (2021), who concluded that different aerosol scenarios in the SWIR do not induce errors greater than 0.2 %. Moreover, since the spectra were observed at low flight altitudes on a rather clear day (see Fig. 1 and Luther et al. 2019), retrieval errors induced by aerosol scattering should be negligible in our scenario as well (also see Fig. 3 and Thorpe et al. 2013; Thompson et al. 2015).

In Fig. 3, the top panel shows the individual components of the monochromatic total transmission for the US-Standard atmosphere, including methane's first overtone of the fundamental vibrational transition $2\nu_3$ (with its P and R branches) around $6000\,\mathrm{cm}^{-1}$ (1560-1660nm, tetradecad band), as well as additional strong absorption lines ranging from $4200-4600\,\mathrm{cm}^{-1}$ (2090-2290nm, octad). The bottom panel illustrates how the observer's coarse spectral resolution smooths the total monochro-
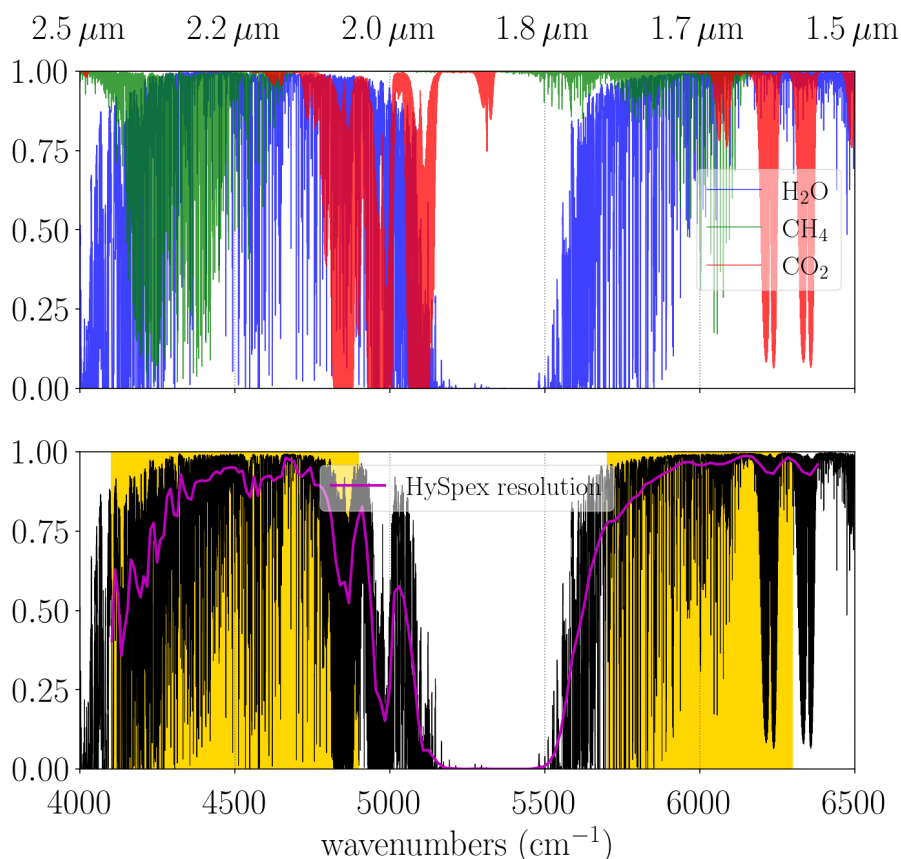
Figure 3. (Top) Monochromatic transmissions of CH_4, CO_2 and H_2O for the SWIR spectral range and a nadir looking observer at 1.5 km at a solar zenith angle (SZA) of 30°. **(Bottom)** Total monochromatic transmission (black) vs degraded to Hyspex resolution (magenta). The spectral intervals used for the CH_4 fit are indicated by the yellow background.

155 matic transmission (shown in black). There are 67 and 28 HySpex pixels detectors used by the retrievals within the range of the 4100–4900 cm^{-1} (4K and 6k spectral windows, respectively .) and 5700–6300 cm^{-1} (6K), respectively (see Fig. 3).

2.2 Model atmosphere setup

The model atmosphere's vertical extent ranges from 0–80 km with 39 levels in total. The atmosphere is composed of pure gaseous layers above altitude $z = 10$ km and layers containing gases and particles below $z = 10$ km. The . The highest vertical resolution is highest in the

160 (plume) layer found in those layers below $z_{\text{pl}} = 2$ km where the enhancement is expected to takes place. The CH_4 optical depth is modeled in terms of divided in two components, i.e., a climatological background and a Gaussian plume

$$\tau_{CH_4} = \tau_{bg} + \alpha\tau \,,$$

where α represents the molecular scaling factor for the plume optical depth while τ_{bg} represents the background.

Although the shape of the plume profile τ_{bg} and a low-level (Gaussian) plume τ. The vertical profile of the initial guess plume is not

165 crucial as the nadir viewing geometry does not allow to retrieve since nadir spectra in the SWIR do not contain sufficient information on the vertical distribution of trace gases in the SWIR (see Buchwitz et al., 2000, Sec. 3)our setup constrains the fit to the lowest atmospheric layer up to 2.0 km (see Thorpe et al., 2014, 5.2)(see Buchwitz et al., 2000, Sec. 3).

The CH_4 background profile as well as the CO_2 background profile are modeled according to the Air Force Geophysical Laboratory (Anderson et al., 1986, AFGL)atmospheric constituent profiles scaled to 1875 ppb and 400 ppm, respectively. The molecules . H_2O as well as

170 the auxiliary parameters temperature and pressure are taken from reanalysis data provided by the National Center for Environmental Prediction (Kalnay et al., 1996, NCEP).

2.3 Beer InfraRed Retrieval Algorithm (BIRRA)

The classical *BIRRA level 2 processor*, developed at DLR, uses the line-by-line forward model Generic Atmospheric Radiation Line-by-line InfraRed Code (Schreier et al., 2014, GARLIC) as forward model and a separate (SLS) or nonlinear least squares

175 solver (NLS) for trace gas retrieval in the SWIR spectral region (Hochstaffl et al., 2018). It has been successfully applied to SCIAMACHY (Scanning Imaging Absorption Spectrometer for Atmospheric Chartography, ; Gimeno García et al., 2011; Hochstaffl and Schreier, 2020) and TROPOMI (TROPOspheric Monitoring Instrument, Hochstaffl et al., 2020) observations. In this study, however, the new Python version of BIRRA is used which is based on Py4CAtS (Python for Computational Atmospheric Spectroscopy, (Schreier et al., 2019)), a Python reimplementation of the validated Fortran code GARLIC (Schreier

180 et al., 2013).

The mathematical forward model $\Phi(\boldsymbol{x},\nu)$ describes the measured intensity spectrum $I(\nu)$ for a nadir looking observer according to

$$\Phi(\boldsymbol{x},\nu) = \frac{r(\nu)}{\pi}\cos(\theta)\,I_{\text{sun}}(\nu)\,\mathcal{T}_m^{\downarrow}(\nu)\,\mathcal{T}_m^{\uparrow}(\nu) \otimes S(\gamma(\nu)) \,, \tag{2}$$

where r refers to the surface reflectivity and θ represents the solar zenith angle. The terms $\mathcal{T}_m^{\downarrow}$ and $\mathcal{T}_m^{\uparrow}$ denote the total trans-

185 mission between Sun and reflection point (e.g. the Earth) and between reflection point and observer, respectively (see Eq. 1). The

The transmission is described by

$$\mathcal{T}_m(\nu; s) = \exp\left(-\sum_m \alpha_m \tau_m(\nu) - \sum_{i>0} a_i \nu^i\right) \exp\left(-\sum_{\mathsf{m}} \alpha_{\mathsf{m}} \tau_{\mathsf{m}}(\nu)\right)., \tag{3}$$

The where the molecular scaling factors α_m adjust initial guess profiles. The simple scaling approach recognizes the significantly under-determined vertical profile information in the observed spectrum and enables an unconstrained least squares fit. All unknown (to be estimated) parameters are composed as elements of collected in the state vector $\boldsymbol{x}$ and include the molecular scaling factors which includes α_m , the aerosol coefficients a_i, and the and the polynomial coefficients for the surface reflectivity r_j (with $j \geq 0$) which is also modeled by a polynomial. Note that since the information of the vertical profile is well under-determined in the observed spectrum scaling factors α_m for the initial guess profiles are retrieved $j \in \mathbb{N}$) (Gimeno García et al., 2011, Fig. 1). Finally, the instrument's spectral response is described by the ISRF S. Its parameters such as the half width γ or a spectral shift can (optionally) be part of the state vector (also see Thorpe et al., 2014, 5.2).

2.3.1 Nonlinear solvers

This study examines various nonlinear retrieval schemes that were are implemented in the BIRRA level 2 processor and are briefly introduced below. Nonlinear least squares methods are iterative and require calculating derivatives for each of the nonlinear state vector elements across the spectral axis, represented by a Jacobian matrix J. Note that $|| \cdot ||$ represents the 2-norm throughout this study.

Nonlinear (NLS) and separable least squares (SLS)

The nonlinear least squares fit minimizes the objective function $\mathcal{L}$ residual norm ($|| \cdot ||$ represents the 2-norm) for given measurements $\boldsymbol{y}$ according to

$$\min_{\boldsymbol{x}} \|\boldsymbol{y} - \boldsymbol{\Phi}(\boldsymbol{x})\|^2 \,,$$

and applies when the model function $\boldsymbol{\Phi}$ is nonlinear in one or more parameters of $\boldsymbol{x}$. according to

$$\min_{\boldsymbol{x}} \|\boldsymbol{y} - \boldsymbol{\Phi}(\boldsymbol{x})\|^2 \,. \tag{4}$$

The so called separable least squares solver SLS splits (separates) the state vector $\boldsymbol{x}$ into nonlinear and linear parameters $\boldsymbol{x} = (\boldsymbol{\eta}, \boldsymbol{\zeta})$ where the elements in $\boldsymbol{\zeta}$ enter the forward model $\boldsymbol{\Phi}$ linearly (see Sec. 2.4.1). The minimization problem is hence given by

$$\min_{\eta, \zeta} \|\boldsymbol{y} - \boldsymbol{\Phi}(\boldsymbol{\eta})\,\boldsymbol{\zeta}(\eta)\|^2 \,. \tag{5}$$

This setup is also known as the Variable Projection (VarPro, Golub and Pereyra, 2003) method where $\boldsymbol{\eta}$ is independent of $\boldsymbol{\zeta}$ in the matrix product $\boldsymbol{\Phi}(\boldsymbol{\eta})\,\boldsymbol{\zeta}(\boldsymbol{\eta})$. The parameters in $\boldsymbol{\eta}$ can hence be fitted in the usual way by means of Gauss–Newton or Levenberg–Marquardt algorithms (Hansen et al., 2013, see)(see Hansen et al., 2013).

Generalized least squares (GLS)

215 ~~To account for correlated errors, a~~ A generalized least squares fit is used to account for correlated errors. The covariance matrix C ~~takes into account the~~ encompasses spectral variations of the scene's background ~~, which includes parts of the flight track that are~~ and the sensor's measurement noise. The motivation is that the matrix compensates for background variations that could mistakenly attributed to methane band absorption. It is computed from background pixels that are assumed to be not affected by the CH_4 plume. ~~To create the matrix C, the location of~~ enhancements. This of course requires some information on the point source~~and wind data~~

220 ~~must be known. The spectral covariance for a given scene is computed to account for possible background variations similar to methane band absorption that could be mistakenly interpreted as a molecular enhancement. Fig. 4 shows the covariance matrices for the methane retrieval intervals.~~ 's location and prevailing wind direction.
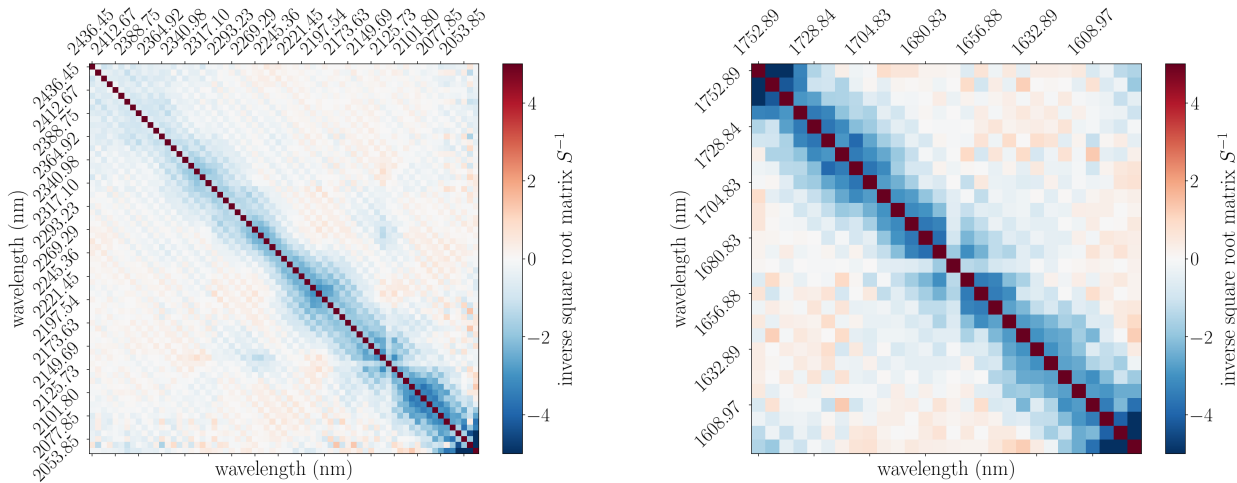
Figure 4. Scene 09 inverse square root matrix of C, **(Left)** 4100-4900 cm^{-1} (4K) and **(Right)** 5700-6300 cm^{-1} (6K) spectral range. The background area was defined outside of the pixels along-track=$(6300, 6670)$, across-track=$(180, 285)$. Note that beside the bad HySpex pixel mentioned in Fig. 2 at $5992.74\,\text{cm}^{-1}$ there appears to be another suspect pixel at $4691.04\,\text{cm}^{-1}$.

The error covariance matrix C is a symmetric positive semi-definite matrix ~~that is precomputed~~ computed for each flight track. ~~To account for correlated errors,~~ Fig. 4 shows the non-negative square root matrix ~~$S = C^{1/2}$ is used to estimate x by minimizing the 2-norm of the weighted residual vector:~~ $S^{-1} = C^{-1/2}$ for the two methane retrieval intervals. In order to reduce fitting errors caused by degeneracies, S^{-1} is included according to

225

$$\min_{\boldsymbol{x}} ||S^{-1}(\boldsymbol{y} - \boldsymbol{\Phi}(\boldsymbol{x}))||^2. \tag{6}$$

~~Scene 09 background covariance matrix for the **(a)** 4100-4900 cm^{-1} (4K, left) and **(b)** 5700-6300 cm^{-1} (6K, right) spectral range. The background area was defined outside of the pixels along-track=$(6300, 6670)$, across-track=$(180, 285)$. Note that beside the bad HySpex pixel mentioned in Fig. 2 at $5992.74\,\text{cm}^{-1}$ there appears to be another suspect pixel at $4691.04\,\text{cm}^{-1}$.~~

230 **2.3.2** **Methane enhancement estimate for nonlinear solvers**

The state vector x for the methane plume fit comprises the scaling factor and a second-order reflectivity polynomial per spectral window. Further parameters were found to be unnecessary as they did not improve the retrieval outcome but rather destabilized the solutions, owing to an increase in the condition number of the Jacobi matrix.

2.3.2 Enhancement estimates for the nonlinear solvers

A scene averaged background spectrum, excluding ground pixels around the suspected CH_4 sources, was is employed to estimate H_2O, CO_2 and CH_4 background concentrations. The CO_2 background level of the scene is inferred from the $1.6\,\mu m$ and $2\,\mu m$ bands via a multi-interval (4K and 6K spectral windows) fit. A scene averaged background For scene 09 and scene 11, a scaling factor of $\tilde{\alpha}_{CO2} = 0.96$ for scene 09 ($\approx 385\,ppm$) and $\tilde{\alpha}_{CO2} = 0.93$ for scene 11 was found($\approx 375\,ppm$) was determined, respectively. Due to the degeneracy between H_2O and the reflectivity polynomial at HySpex's spectral resolution, the scene averaged H_2O scaling factor should be viewed as effective parameter that partly captures constitutes an effective parameter partly capturing low frequency components in the spectrum. The scene averaged CH_4 background profile was found to be within 5 % of the initial guess of 1875 ppbv, hence it was maintained and not is not (pre)scaled.

The decision to exclude aerosol parameters from state vector x for the CH_4 plume fit was encouraged by findings from Borchardt et al. (2021), who concluded that different aerosol scenarios in the SWIR do not induce errors greater than 0.2enhancement fit comprises the CH_4 scaling factor and the coefficients for a second-order reflectivity polynomial per spectral interval $x = (\alpha, r_0, r_1, r_2)$. In this setup the parameter α only applies to the plume component (up to 2.0 %. Moreover, since the spectra were observed at low flight altitudes on a rather clear day (see Fig. 1 and Luther et al. 2019), retrieval errors induced by aerosol scattering should be negligible in our scenario as well (also see Fig. 3 and Thorpe et al. 2013; Thompson et al. 2015) . Nonetheless the study accounts for light path modifications in the reported km) of the CH_4 estimates by using the scene average α_{CO2} scaling factor from above. optical depth

$$\tau_{CH_4} = \tau_{bg} + \alpha\,\tau\,. \tag{7}$$

This setup was found robust toward lower SNR values and less susceptible to correlations among state variables, which in turn enhances the condition number of the Jacobian matrix.

The actual CH_4 column total column is then given by the background concentration plus the retrieved enhancement and includes corrections for light path modifications via the prefitted scene averaged background CO_2 $\tilde{\alpha}_{CO2}$ given by given by

$$N_{CH4} = N_{bg} + \frac{\alpha}{\tilde{\alpha}_{CO2}}\,\hat{N}_{pl}(z_0)\,, \tag{8}$$

with

$$\hat{N}_{pl}(z_0) = \int_{z_0}^{z_{pl}} n_{pl}(z)\,dz\,, \tag{9}$$

and z_0 representing the bottom of the atmosphere . Note that this and n_{pl} the plume's number density. This approach assumes that the CO_2 profile upon which $\tilde{\alpha}_{CO2}$ was estimated corresponds to the true profile and that $\tilde{\alpha}_{CO2}$ is 1 in absence of scattering. The actual retrieval fits the methane enhancement factor along with a second order reflectivity polynomial so that the state vector is given by $x = (\alpha, r_0, r_1, r_2)$. This setup is found robust toward lower SNR values and less prone to correlations across state variables.

2.4 Linear solvers

In contrast to nonlinear fitting schemes, linear solvers for x can only be used when equations can be expressed as a linear combination of the variables in x. To utilize such methods, it is usually required to linearize the forward model with respect to the variables of interest. The solvers can be split into two groups, i. e., one that take background statistics into account (MF and SVD) and the two others that do not (LLS and SSD).

2.4.1 Linear least squares (LLS)

The LLS method uses a linear fitting scheme to estimate the parameter (see Eq. 7). Assuming that the increase in optical depth caused by the plume, τ, is relatively small, the BIRRA forward model from Sec. 2.3 is linearized with respect to α by approximating the transmission spectrum of the plume by Taylor expansion according to

$$\exp(-\tau) \approx (1 - \alpha\tau) . \tag{10}$$

The linear least squares problem of M measurements can then be formulated according to

$$\min_{x} ||y - \Phi x|| \tag{11}$$

where the model functions in Φ for the linear parameters of the state vector $x = (r_0, b_0 = r_0\,\alpha)$ $x = (r_0, r_0\,\alpha)$ are given by

$$\phi_1 = \frac{\cos(\theta)}{\pi} I_{\text{sun}} \mathcal{T}^{\downarrow} \mathcal{T}^{\uparrow} \otimes S, \tag{12}$$

$$\phi_2 = -\frac{\cos(\theta)}{\pi} I_{\text{sun}} \mathcal{T}^{\downarrow} \mathcal{T}^{\uparrow} \tau \otimes S. \tag{13}$$

It is important to note that with in this setup the reflectivity coefficient r_0 is present in both two elements of the state vector. In order to avoid this degeneracy and allow for higher order reflectivity polynomials in the fit, which are required for large spectral intervals, the retrieval is performed in two steps. In a first step First, only the reflectivity coefficients are fitted while in a second step only α is estimated with the prefitted reflectivity coefficients given pre-fitted reflectivity coefficients provided as input. This setup allows fits for an increased spectral interval. In addition, the setup allows for spectral separation The setup can be complemented by de-weighting individual pixels in the albedo fit that are impacted by methane. This basically ensures that the reflectivity coefficients can be fitted outside the absorption bands of the target, and then the enhancement factor can subsequently be estimated from the range where absorption occurs. This approach minimizes interference between the two fits, preventing the reflectivity polynomial from capturing absorption of CH_4.

Another aspect that should be kept in mind is that that since $1 - \alpha\tau \leq \exp(-\alpha\tau)$ for $\alpha \geq 0$ the linearized model underestimates the CH_4 enhancement for a given optical depth τ compared to the nonlinear setup (forward plus inversion). However, the setup should be sensitive enough to yield elevated methane levels. .

2.4.2 Matched Filter (MF)

The MF is a well-established method for estimating molecular concentration enhancements from hyperspectral sensors, with numerous studies supporting its effectiveness (Theiler and Foy, 2006; Villeneuve et al., 1999; Funk et al., 2001; Thorpe et al., 2013; Thompson et al., 2015) (Villeneuve et al., 1999; Funk et al., 2001; Thorpe et al., 2013; Thompson et al., 2015). The linear enhancement factor estimate is

derived is inferred by perturbing an average (background) radiance spectrum $\boldsymbol{\mu}$ with a known target spectrum $\mathbf{t}$. The approach is analogous to that used by Thompson et al. (2015), where CH_4 enhancements are estimated by linearly scaling a target signature that perturbs the mean radiance

$$\alpha_i(\boldsymbol{y}) \; = \; \frac{(\mathbf{t}(\boldsymbol{\mu}))^{\mathrm{T}} \, \mathsf{C}^{-1} \, (\boldsymbol{y}_i - \boldsymbol{\mu})}{\sqrt{(\mathbf{t}(\boldsymbol{\mu}))^{\mathrm{T}} \, \mathsf{C}^{-1} \, (\mathbf{t}(\boldsymbol{\mu}))}} \, . \tag{14}$$

This equation constitutes the linear minimizer that solves the Gaussian log-likelyhood log-likelihood

$$\min_{\alpha_i} ||\mathsf{C}^{-1/2} \boldsymbol{d}||^2 \quad \text{with} \quad \boldsymbol{d} = \boldsymbol{y}_i - (\boldsymbol{\mu} + \alpha_i \mathbf{t}(\boldsymbol{\mu})) \quad \text{and} \quad \mathbf{t}(\boldsymbol{\mu}) = -\boldsymbol{\mu}\,\boldsymbol{\tau}. \tag{15}$$

The method assumes that the measured spectrum can be represented as a linear superposition of the CH_4 plume's optical depth and the mean unperturbed radiance $\boldsymbol{\mu}$ and tests an observed vector $\boldsymbol{y}_i$ $\boldsymbol{y}_i$ against a base vector while accounting for the background covariance C. Note that the The mean background spectrum $\boldsymbol{\mu}$ and C were are computed per scene and the inverse covariance C^{-1} is approximated by decomposing C into eigenvalues and eigenvectors (Thompson et al., 2015, Eq. 6-8)(Thompson et al., 2015, Eq. (6)-(8)).

In order to get a more accuratetarget spectrum estimateimprove accurate, a per pixel estimate of the target spectrum was measurement target spectrum is computed which accounts for the pixel's albedo (Foote et al., 2020, II. Methods, C.). This albedo normalized matched filter includes an albedo factor r_i for each measurement spectrum according to

$$\boldsymbol{d_r} = \boldsymbol{y}_i - (\boldsymbol{\mu} + r_i\,\alpha_i\,\mathbf{t}(\boldsymbol{\mu})) \quad \text{with} \quad r_i = \frac{\boldsymbol{y}_i^{\mathrm{T}}\,\boldsymbol{\mu}}{\boldsymbol{\mu}^{\mathrm{T}}\,\boldsymbol{\mu}} \tag{16}$$

However, the MF method has its limitations, e.g. it suffers from heterogeneous background and correlation between the plume and the background which limits the detection quality even for strong plumes (Theiler and Foy, 2006). According to Guanter et al. (2021), the classical matched filter is relatively sensitive to surface albedo which could be mitigated a way to mitigate the effect is by k-means clustering of the scene. This approach reduces within-class variance, which in turn should minimize the albedo sensitivity of α. In the so called so-called cluster-tuned matched filter, instead of computing a single background covariance statistic, a per-cluster background statistic C_i is computed for each cluster i, determined by k-means clustering (Thorpe et al., 2013; Nesme et al., 2020).

2.4.3 Singular Value Decomposition (SVD)

The retrieval of methane enhancements from hyperspectral AVIRIS data using singular vectors of the observed spectrum plus a target signature was first demonstrated by Thorpe et al. (2014). The SVD method is well-suited for parameter estimation from moderately resolved spectral data because it allows to consider only the most significant components of the spectrum while preserving the main spectral information.

In this study the The orthogonal singular vectors are obtained from HySpex spectra that are not impacted by the plume. The matrix containing the scene's log-space background spectra I_{bg} was is decomposed into USV^{T}, where $U \in \mathbb{R}^{m \times m}$ and $V \in \mathbb{R}^{n \times n}$ are unitary matrices, and $S \in \mathbb{R}^{m \times n}$ is a diagonal matrix. The target spectrum signature (spectrum) is represented by the CH_4 plume's optical depth $\boldsymbol{\tau}$ which was is computed with Py4CAtS.

The basic idea is analogous to the MF, i. e., to represent the general variability in spectral radiance by a linear combination of singular vectors and a target signal. The minimization problem is then given by

$$\min_{\boldsymbol{w}} ||\boldsymbol{y} - \mathsf{A}\,\boldsymbol{w}||^2 \quad \text{with} \quad \mathsf{A}\,\boldsymbol{w} = \sum_{k}^{N} \boldsymbol{u}_k\,\boldsymbol{w}_k + \boldsymbol{t}\,\boldsymbol{w}_{\text{CH4}} \tag{17}$$

where A represents the concatenated matrix of the first N columns of the unitary matrix U . (see Fig. 5). The vector $\boldsymbol{w}$ contains the corresponding weights with $\alpha = \boldsymbol{w}_{\text{CH4}}$ scaling the contribution of enhanced methane in the lowest atmospheric layers $\boldsymbol{t} = \boldsymbol{\tau}$. In the cluster-tuned variant the background spectra are clustered by k-means and the SVD is performed for each cluster separately and the . The respective base vectors per cluster were are then used in the linear fit.

(a)   (b)
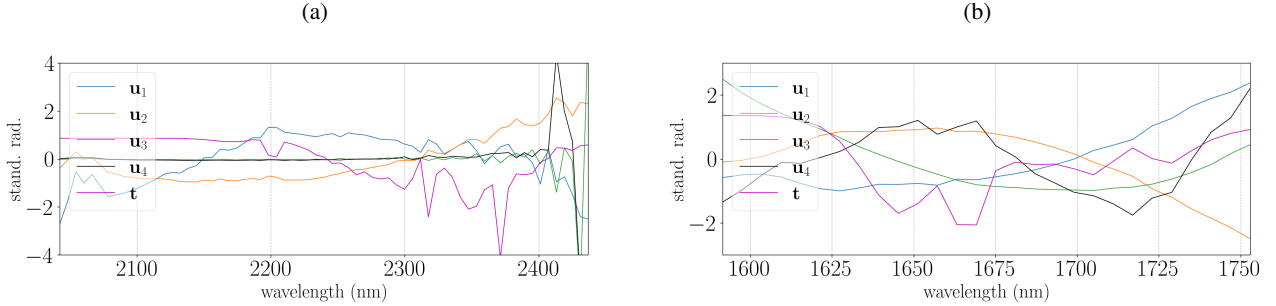
Figure 5. Standardized singular vectors and the methane plume's target signature $\mathbf{t}$ in 4K (left) and 6K (right) spectral intervals, respectively. Standardization removes the mean and scales to unit variance. While the The $\boldsymbol{u}$ vectors were yielded from are defined by the SVD and the vector $\mathbf{t}$ was computed with vector by the radiative transfer model Py4CAtS. Modelling the plume's optical depth with the same tools and for an equivalent setup (< 2 km) is crucial for comparability with the nonlinear BIRRA setups.

2.4.4 Spectral signature detection (SSD)

A straightforward approach for detecting spectral to identify methane absorption is the SSD fit which compares the ratio of spectral residual norms to produce a score. Unlike other methods, this approach does not require any radiative transfer calculations, look-up tables, or initial guess information, only calibrated sensor data for a specific interval.

The algorithm is based on a simple polynomial fit of spectral pixels and the calculation of spectral residuals. The idea behind this method is similar to the continuum interpolated band ratio (CIBR) from Green et al. (1989) and Thompson et al. (2015, Eq. 2) Thompson et al. (2015, Eq. (2)), which also measure measures absorption depths (Pandya et al., 2021). The method splits the spectral interval into pixels where CH_4 absorbs is absorbed and where it does is not (or only weakly, also see the LLS method) and by linear least squares a . A polynomial of degree P is fitted to the M out-of-band pixels

$$\min_{\boldsymbol{x}} ||\boldsymbol{y} - \boldsymbol{p}(\boldsymbol{x})||^2 \quad \text{with} \quad p(\boldsymbol{x}, \nu_i) = \sum_{j=0}^{P} \alpha_j\,\nu_i^j, \qquad j = 1, 2, \cdots, P \quad \text{and} \quad i = 1, 2, \cdots, M. \tag{18}$$

Next the residual norms for the in- and out-of-band pixels are computed and the ratio formed $r_{\text{in}}/r_{\text{out}}$ which provides an . The ratio of the residual norms yield a absorption band depth score for each observation , i. e., the score which indicates variations in the CH_4 absorption if given taht the in- and out-of-band pixels were properly chosen.

The algorithm constitutes a fast detection scheme which can also be applied for real-time detection of enhancements, e. g., determine whether or not a CH_4 ventilation shaft is active at the time of instrument overpass. When a zero order polynomial is used for the out-band fit, the method is comparable to the CIBR algorithm. However, by using higher order polynomials, the method can model the surface reflectivity and other interfering species more precisely, especially over larger spectral intervals.

3 Results

This section presents the results for the CH_4 estimates from various retrieval methods over the Pniovek V shafts. The site was selected since it showed significant methane releases during the times of overpass in flight track 9 (scene 09)and flight track 11 on June 07, 2018 (see Fig. 1). The results presented subsequently focus on measurements from scene 9. shaft(s). Except otherwise stated, the retrievals were performed on 3×3 pixels averaged spectra in order to increase the signal-to-noise ratio and thereby reduce scattering clutter of the CH_4 fits across pixels.

3.1 NLS and SLS fits

Figures ?? and ?? show Figure 6 shows the results of the classical BIRRA NLS fit. The position of the source is indicated by the intersection of the dashed line. The fits reveals a significant enhancement of CH_4 in both spectral intervals above and downwind of the ventilation shaft. However, the bias caused by different surface types is opposite in the 4K and 6K intervals, which is worth mentioning. An analogous behavior is observed for both BIRRA configurations exhibit biases, with the SLS fit although it is more sensitive to variations in the background. displaying a somewhat more pronounced sensitivity to surface variations (therefore not shown). As depicted in Fig. 6 the combination of multiple spectral intervals can alleviate these adverse effects to a considerable extent and the downwind shape of the plume is captured better (see Table 2).
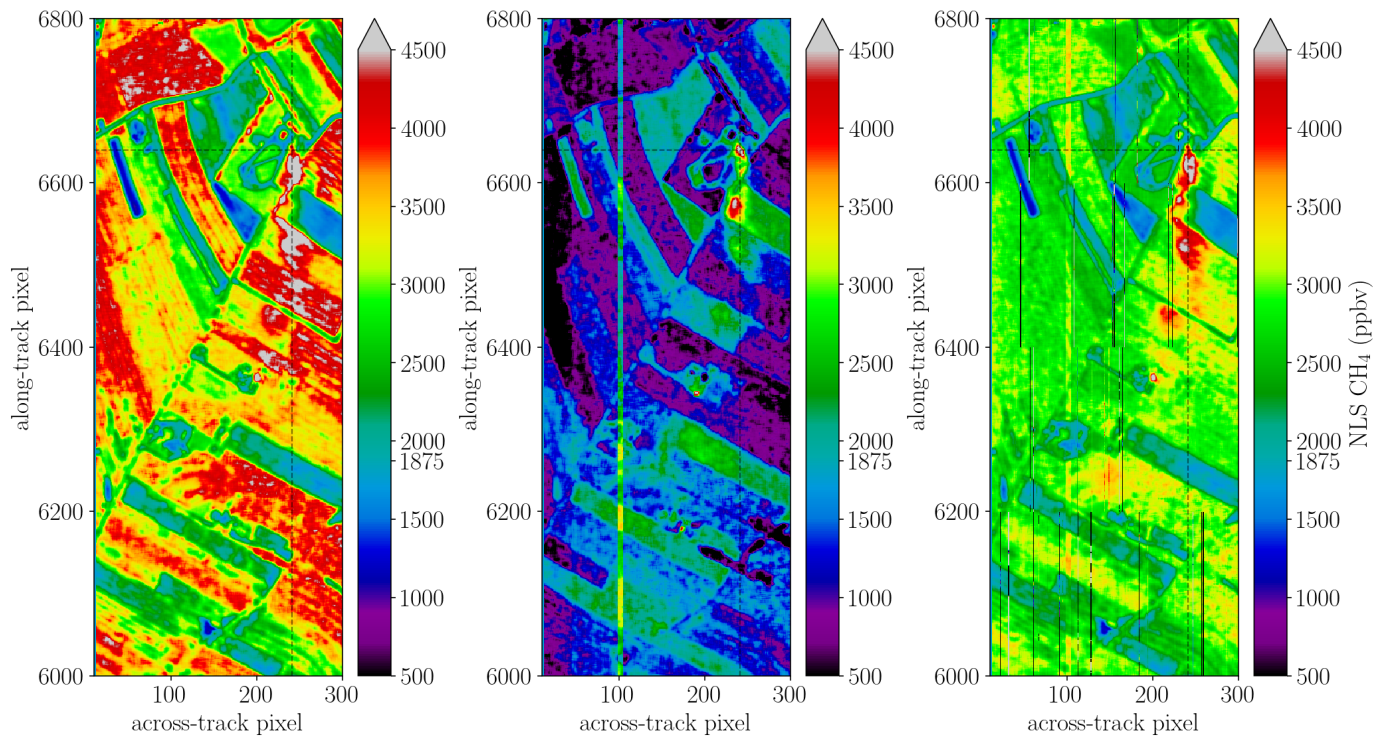
Figure 6. Methane enhancements for 3×3 spatially averaged HySpex observations in the (a) multi-interval fit (combining 4K and 6K ranges). (b) shows the result for the **(Left)** 4150–4900 cm^{-1} (4K) interval , while (c) depicts enhancements inferred from and the **(Center)** 5700–6300 cm^{-1} (6K) range. **(Right)** Multi-interval fit, i.e., combining the 4K and 6K ranges. Note that the latter former two fits suffer from albedo correlations with the target methane in opposite direction.

The multi-interval retrieval shown in Figure **??** improves the result by reducing albedo-induced variabilities on the target, however the retrieval still suffers from surface-correlated offsets but to a much smaller degree than single-interval fits. The maximum enhancements and plume pattern are similar, but the downwind shape of the plume is better captured (see Table 2).

360

3.2 GLS fits

Figure 8 displays the retrieved columns using the generalized least squares (GLS) fit from averaged spectra for scene 09 in the 4K and 6K intervals. Compared to other methods, it reduces the correlation between the methane enhancement and surface reflectivity significantly, resulting in a more distinct plume signal and less background clutter.
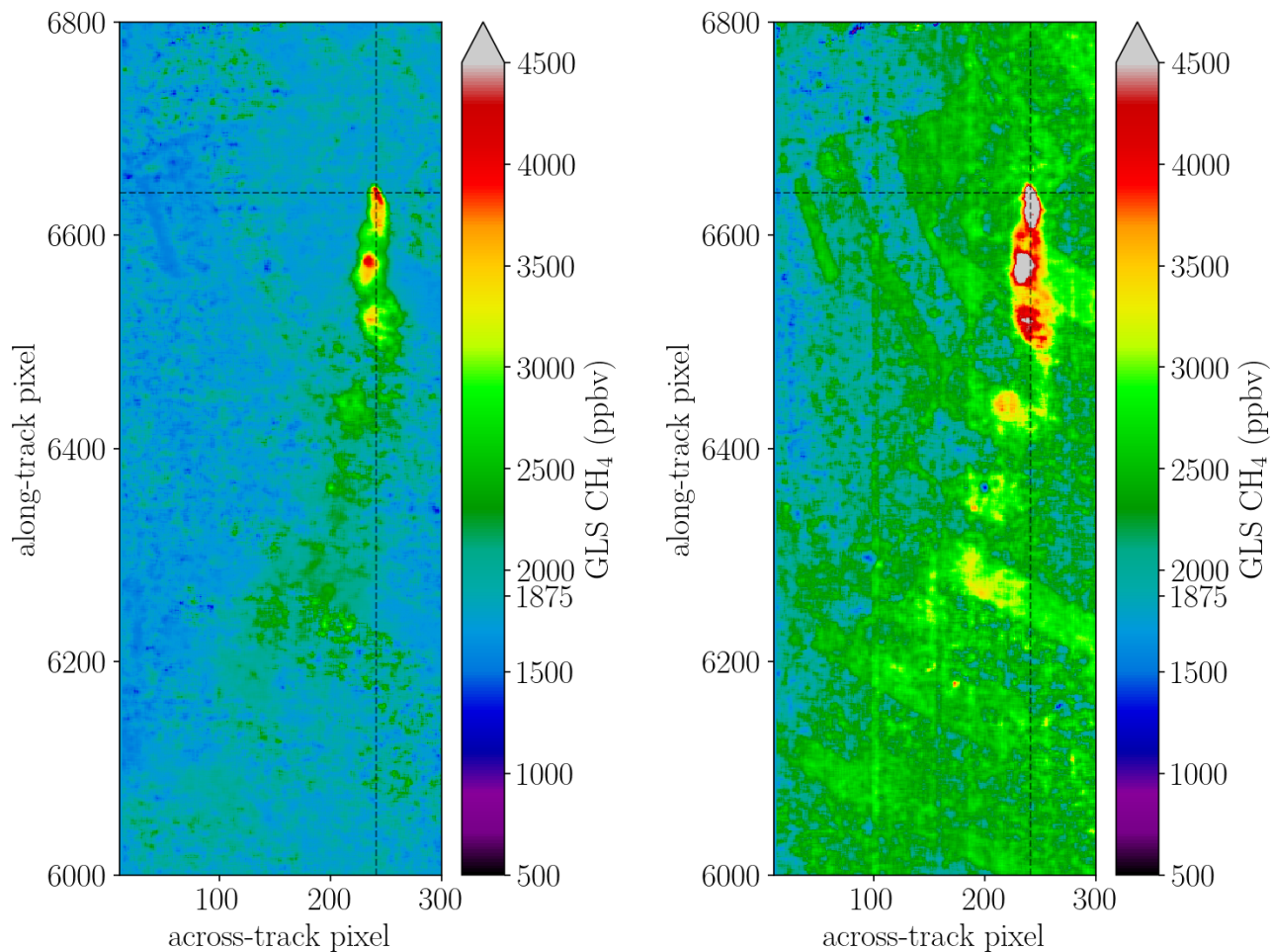
Figure 7. Methane plume depicted for the single window covariance weighted fits for scene 09. The background pixel concentration is rather stable in the 4K interval depicted in (a) **(Left)** while there is still some overestimation of CH_4 in the 6K range in (b)**(Right)**.

Figure ?? 8 shows the multi-window covariance weighted GLS fits for scene 09 and 11. In both cases the retrieval yields a distinct plume that separates well from background clutter. Figure ??shows The figure depicts the impact of decreasing ground pixel resolution (from higher altitudes) on the inferred concentrations as enhancements are less pronounced . However, partly for scene 11. However, this could also partly be attributed to less a decreased amount of emissions since the observation was taken at another point in time. Also Furthermore, winds could have changed as the plume's shape is different compared to scene 09 in Fig. ??. 09.
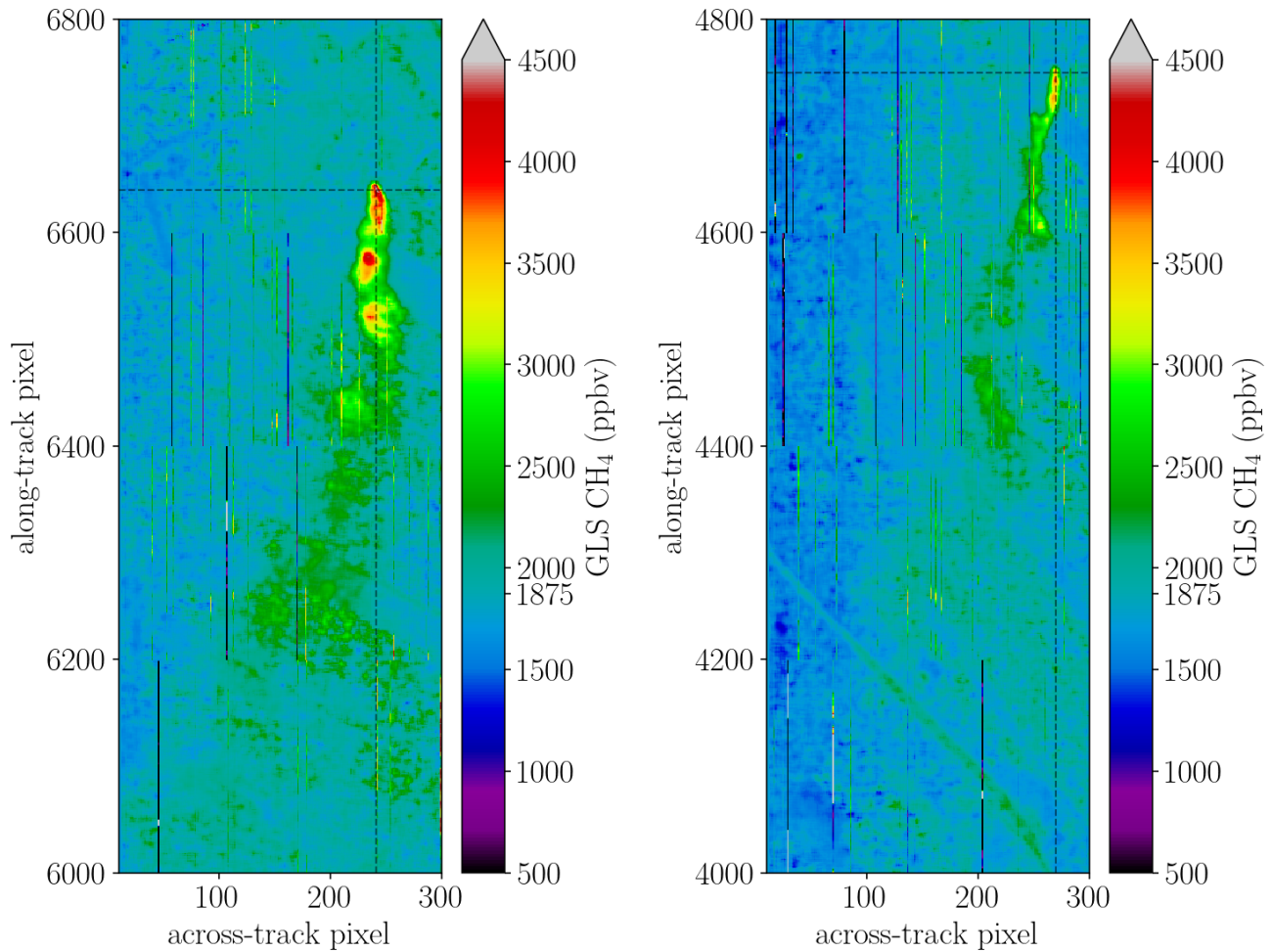
Figure 8. Best results are acquired **(Left)** Multi-window (4K and 6K) retrieval output for GLS setups. **(a)** depicts the enhancements for scene 09 while **(b)** depicts the output and **(Right)** enhancements for scene 11. The stripe pattern in the along track direction is a multi-window retrieval artefact.

Figure 9 depicts the fits from individual (non-averaged) HySpex spectra for scene 09 and 11 for the GLS multi-window retrieval setup. The single pixel total columns are more affected by retrieval noise caused by the lower signal-to-noise ratio (SNR) which varies significantly over different surface-types. However, the method still identifies elevated methane concentrationsand is moreover only minor affected by albedo correlations. Also note that the maximum enhancements are more pronounced, particularly in scene 11 where further degrading ground pixel resolution by spatially averaging apparently has somewhat greater impact on downwind concentrations. .

375
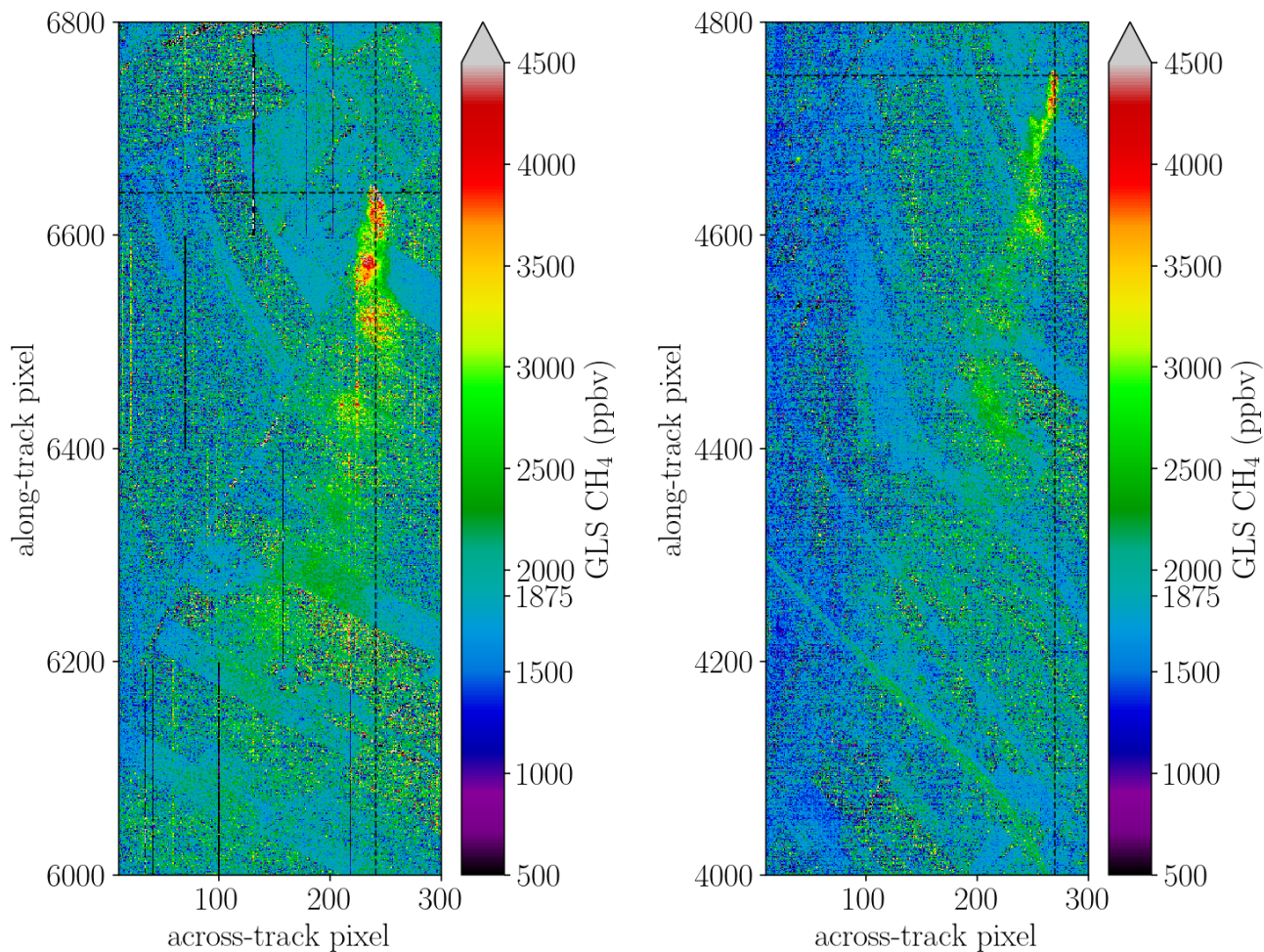
Figure 9. Same as Fig. **??** but for single Single pixel spectra (not 3 × 3 averaged). Again **(a)** depicts depicted for **(Left)** scene 09 results and **(b) (Right)** scene 11. Retrieval noise is significantly depending on the underlying surface.

3.3 MF fits

The classical and the albedo normalizedmatched filter is albedo normalized, cluster-tuned and classical matched filters are examined for scene 09. Both Figure 10 shows that all three variants are able to identify the methane plumebut the and as shown in Fig. 10, the , although absolute CH_4 concentrations differ in certain parts of the scene. The cluster-tuning is beneficial in reducing the interference of the plume signal with surface reflectivity. MF variant in middle panel yields more homogeneous enhancements downwind across various surface types but pixels along class boundaries such as streets show some artefacts.
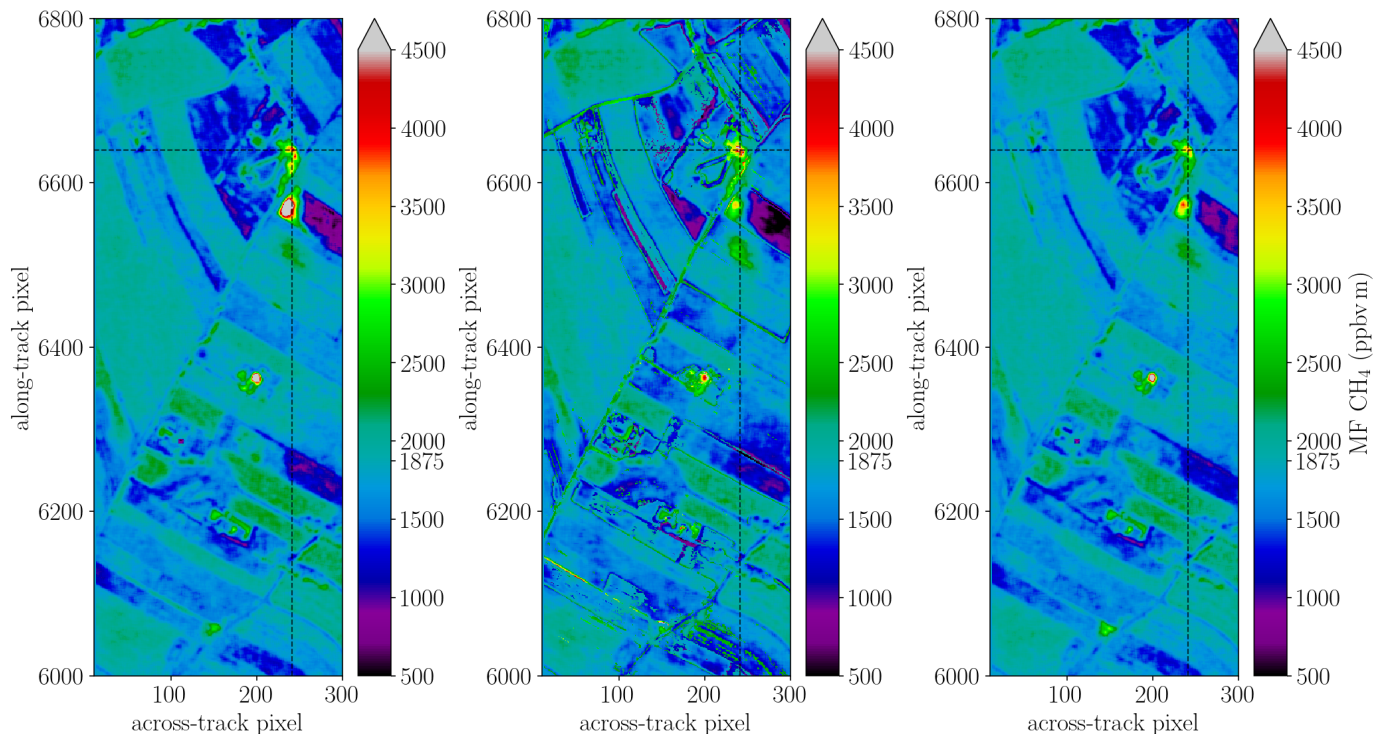
Figure 10. (a) **(Left)** Albedo normalized variant of the MF(b) , **(Center)** the cluster-tuned MF variant and (c) **(Right)** the classical MF fits in fit shown for the 4K interval (4100-4900 cm^{-1}), respectively.

3.4 SVD fits

The SVD-based retrieval method illustrated in Fig. 11 is able to identifying identify elevated levels CH_4 in the HySpex spectrum. The method yields consistent results for both spectral intervals employing four base vectors and the CH_4 Jacobian for the lowest 2km (see Fig. 5). Including more than four base vectors significantly increase increases the condition number of A as columns column five interferes with the methane signal. The albedo normalized MF variant yields somewhat larger values depicted in Fig. **??** compared to the classical variant in Fig. **??**. Cluster-tuning also improves the results in Fig. **??** but since the MF already takes background covariance into account the impact is small.

The plume was plume is also identified for the purely ''data-driven' approach, i. e.,' approach, where the base vector that mimics mimicking the CH_4 absorption, i. e., (the fifth column in U) is used instead of the CH_4 spectrum. This approach does hence Thus, this approach does not require any forward model and is hence purely data-driven. Cluster-tuning in general improves the fit due to a reduction in variance within each cluster, however, the results become more sensitive to the selected number of base vectors. It was found that within a cluster the number of base vectors required to ensemble resemble A should be reduced.
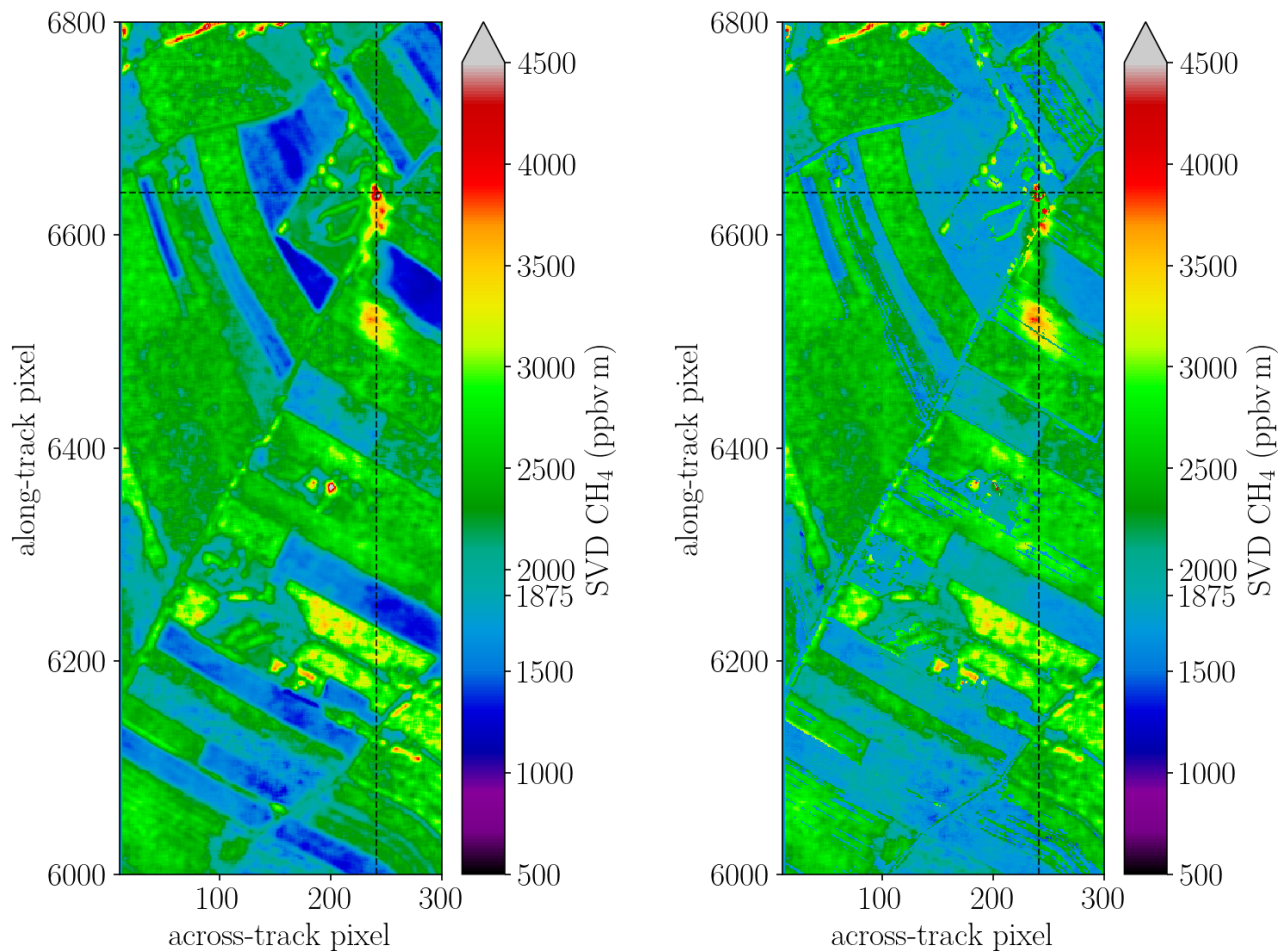
Figure 11. (a) **(Left)** Standard SVD fit and (b) **(Right)** background cluster-tuned SVD, both for the 6K spectral range. Three clusters reduce background clutter but suppresses some enhancements close to the source. However, also false positives like the spot around the coordinate (200,6350) are diminished.

3.5 LLS fits

The results for the linearized BIRRA fits are shown in Fig. 12. The method Linear least squares is able to identify CH_4 enhancements, although it
395   differs significantly in the absolute values in the 4K (Fig. 12) and 6K (spectra range (see Fig. 12)spectral range. As pointed out in Sec. 2.4.1, the method is prone to underestimate enhancements. Moreover, the selected weights for the reflectivity coefficients fit were found to impact the CH_4 result. However, for the sake of simplicity and since the optimal selection of weights was not clear at the time of writing initially, no weighting was applied. Its results turned out to be sensitive to which deweight the impacted pixels. Similar to its nonlinear counterpart (NLS) the fit is also affected by albedo related offsets in opposite directions in the two intervals.
400   However, relative enhancements between plume and background values are rather similar.
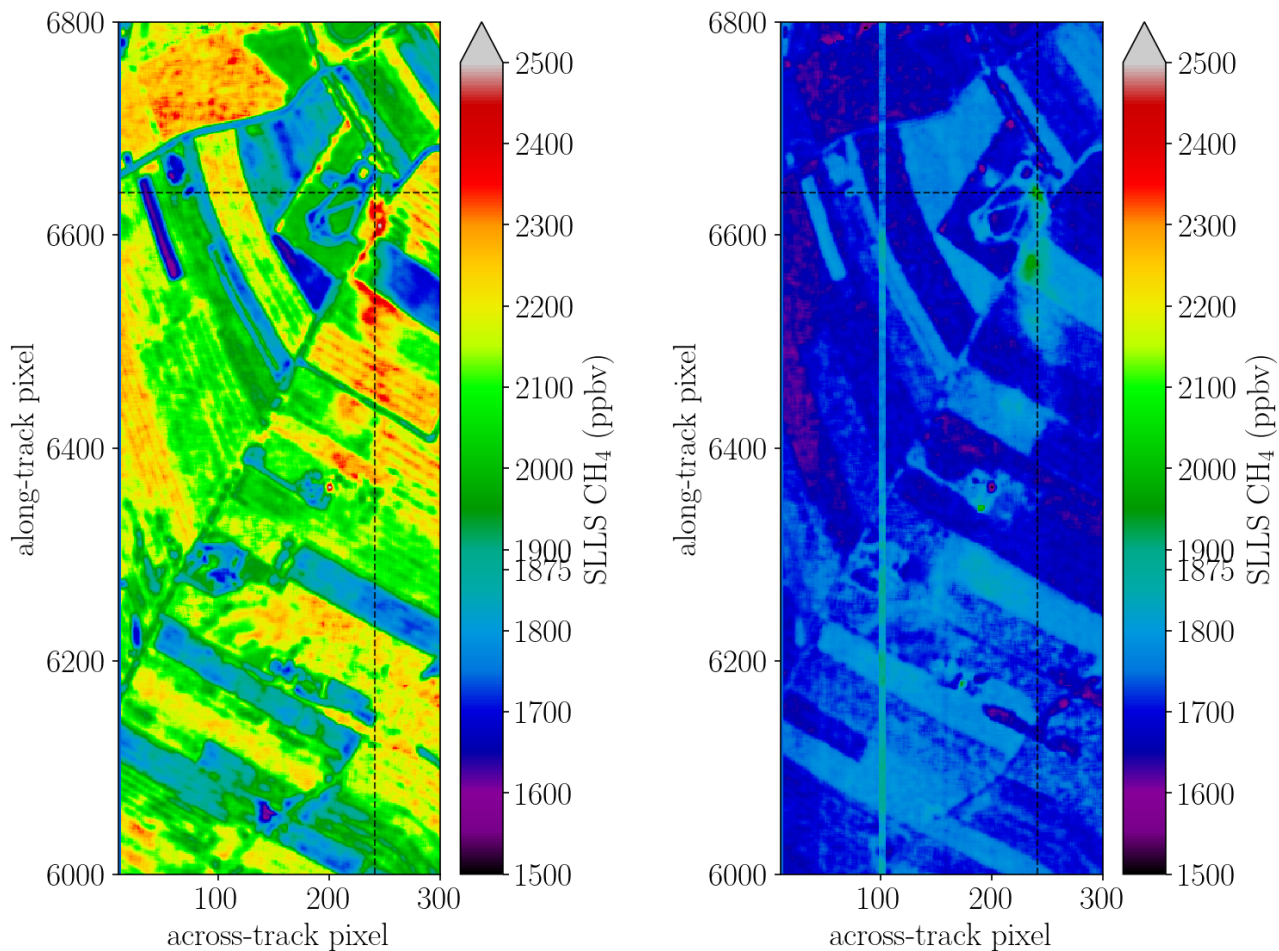
Figure 12. CH$_4$ enhancements for scene 09 estimated with the linear forward model LLS setup. The results in Fig. (a) **(Left)** show the results for the 4K spectral window while Fig. (b) **(Right)** shows the 6K outcome. In the latter method, the methane enhancements are less pronounced, but the reflectivity related bias is also smaller.

3.6 SSD fits

In Fig. 13 results for the SSD method are shown. A second order polynomial is fitted in Fig. **??** while a constant is used in Fig. **??**. The result show that relative variations are more pronounced in the zero-order fit while the higher order fit better captures the downwind plume by suppressing background clutter.

405 It is important to note that the method yields better results for the 6K absorption since the 4K absorption features are distributed over a larger spectral range which causes more uncertainty in the out-of-band polynomial fit since many pixels need to be omitted.
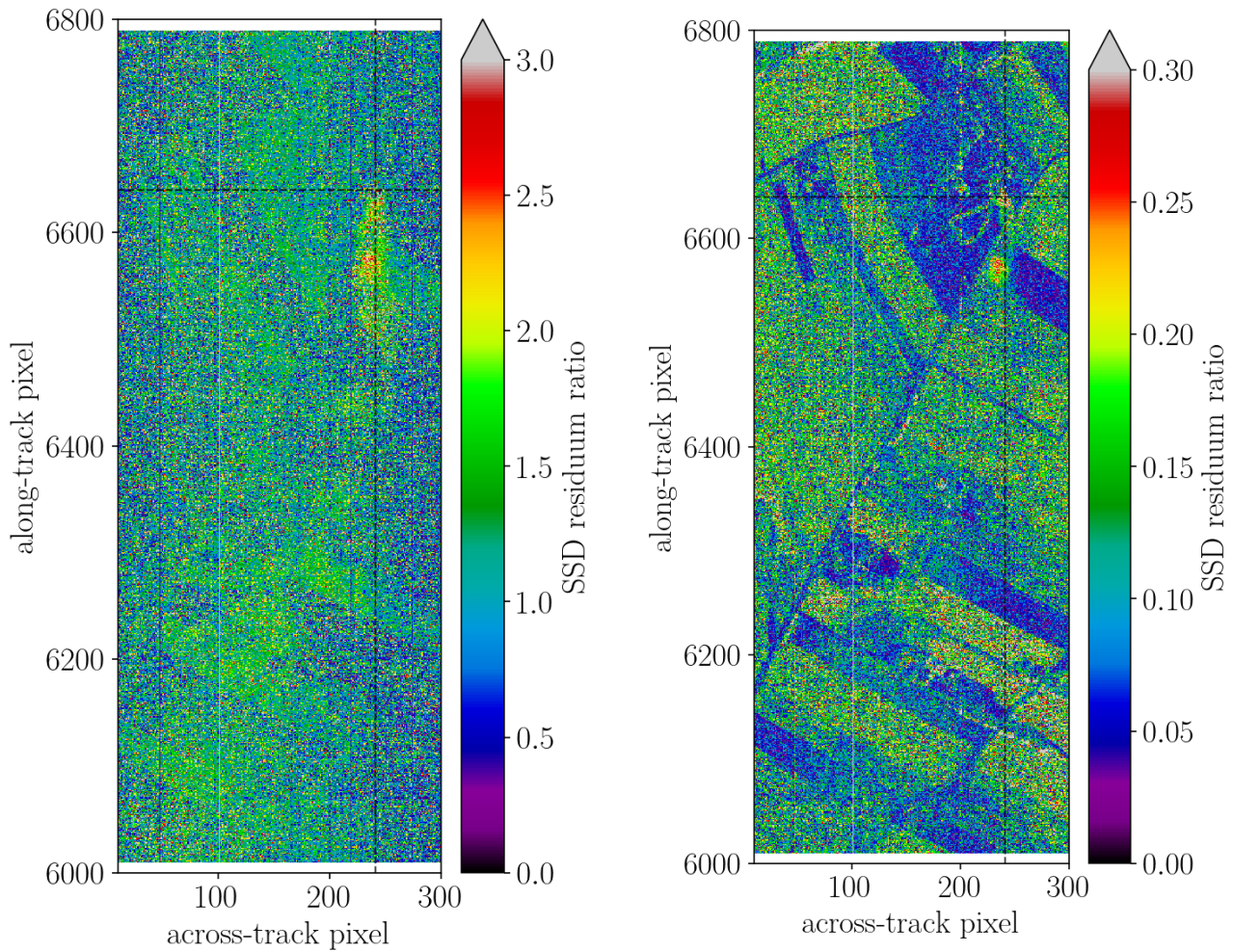
Figure 13. The ratio of the spectral residuals in the 6K range for the in- and out-band pixel are depicted. In (a) **(Left)** the in-band residuals were computed ~~towards~~ with respect to a quadratic polynomial while ~~in (b)~~ on the **(Right)** a constant was used.

3.7 Statistical significance of results

In order to provide a more quantitative measure on the quality and confidence of the fits a Student's t-test was applied to the results (Varon et al., 2018). The test helps to measure how well the plume is represented with respect to the background for a given retrieval setup. This is accomplished by testing for pixels that contradict the null hypothesis(background pixel) and hence should , which assumes that all pixels belong to the plume. background (methane concentration). Moreover, samples need to be independent and identically normal distributed (Bruce et al., 2020).

The method assumes that the background samples are normal distributed with equal variance, and that they are independent (Bruce et al., 2020). The null hypothesis was rejected for significance levels 0.01 at the 1 % significance level which can be considered a strong evidenceagainst the null hypothesis.

Although some fit results may ask for a tighter significance level in the t-test to isolate the plume and get rid of most outliers, for the sake of comparison 0.01 1 % is used throughout this study.
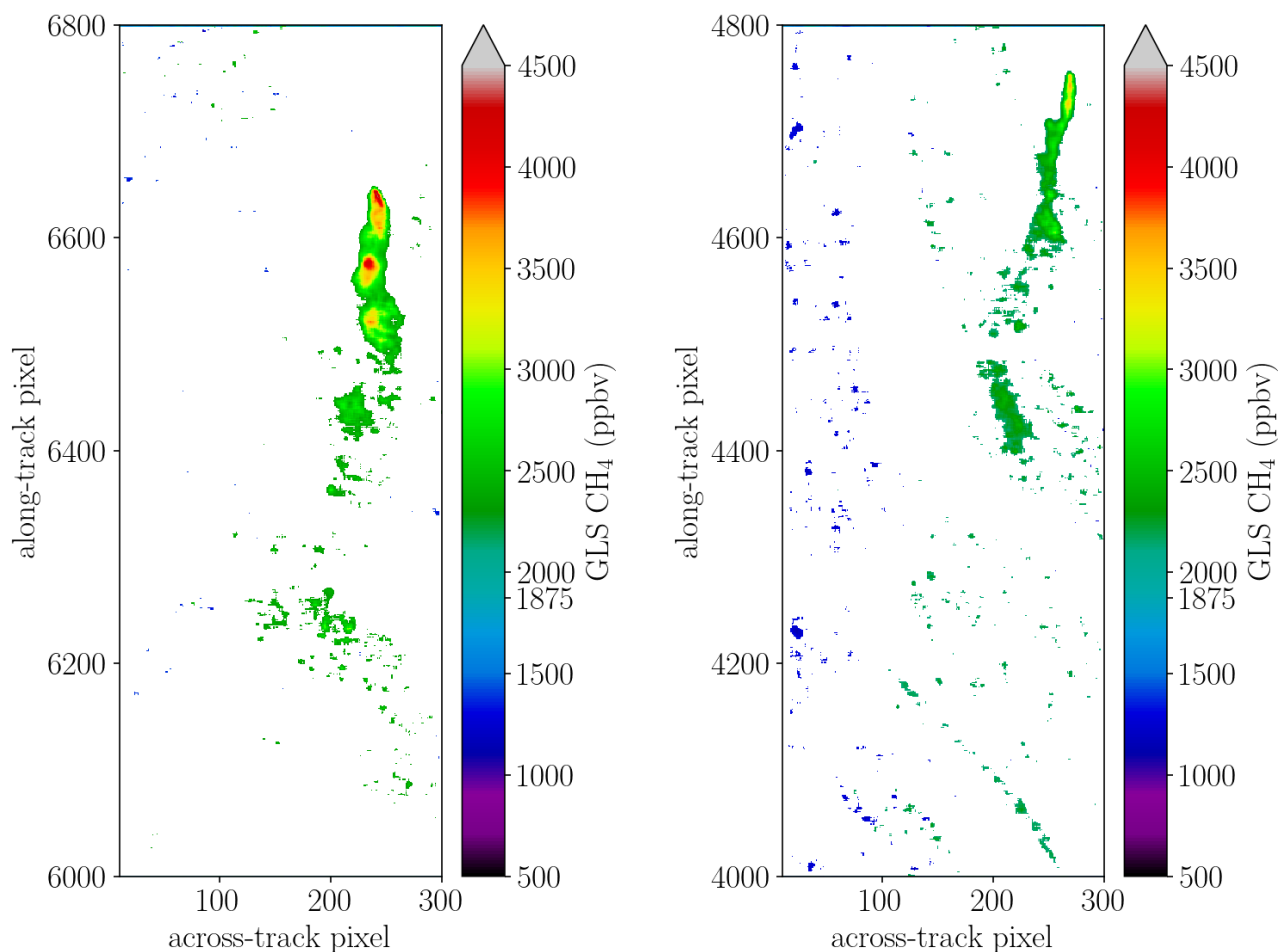
Figure 14. Plume pixels according to the Student's t-test for the nonlinear multi-window GLS fit. (a) **(Left)** Shows scene 09 while (b) **(Right)** displays scene 11.

Figure 14 depicts the result of the t-test applied to the retrieval output for scene 09 and 11 from the covariance weighted nonlinear solver (GLS) in the 4K range. The plume is well pronounced and the test is able to isolated isolate enhanced CH_4 values from the background. In particular, the higher ground-resolution scene 09 shows almost no outliers at the selected significance level meaning indicating that the depicted values occur only in $\leq 1\%$ of the casesgiven , assuming the null hypothesis (background methane concentrations) is trueto hold. Moreover, finding such extreme values by chance in such a pattern is even more likely and hence the result gives confidence that the is is a methane plume originating at the source that is transported downwind.
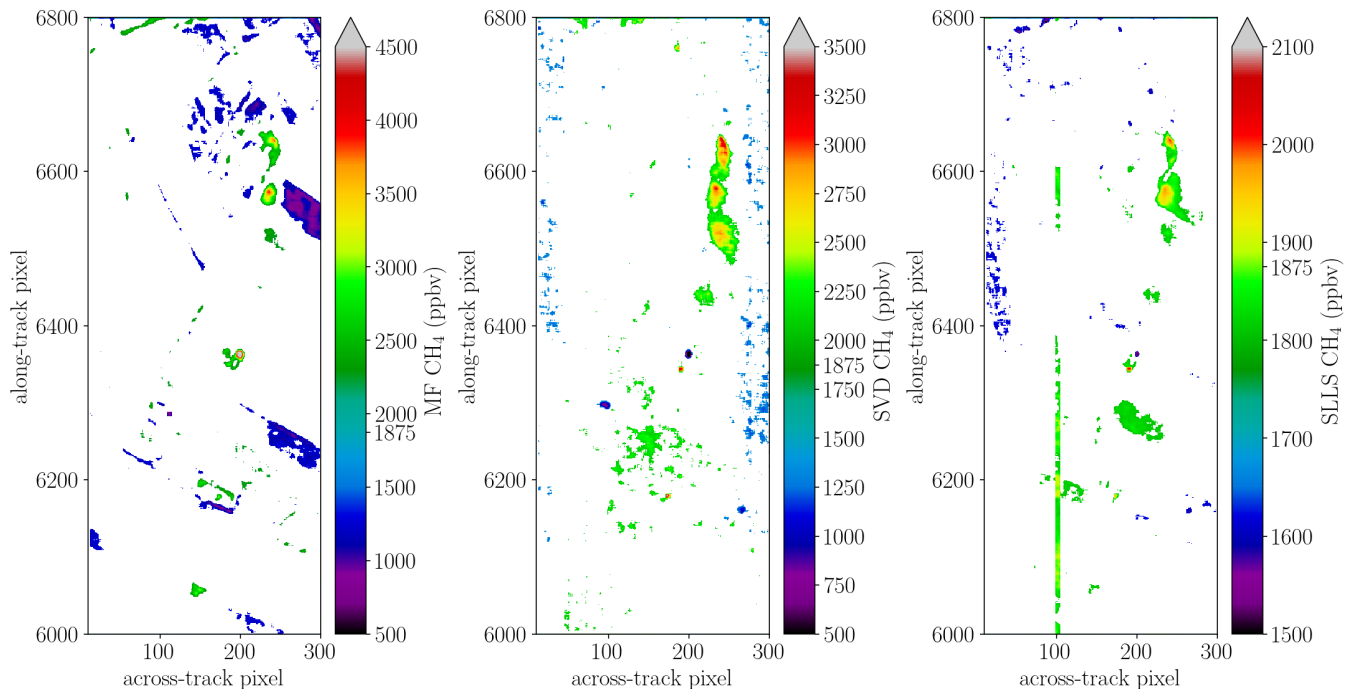
Figure 15. Plume pixels identified by the t-test in scene 09 for the different linear schemes. Note that the color scale was adapted. **(a) (Left)** Classical MF output from the 4K range, **(b) (Center)** displays plume pixels accoding to the SVD method in the 6K interval, and **(c) (Right)** presents the SLLS fit in 6K.

The Student's t-test was also applied to the linear solvers and the results are shown , with results reported in Fig. 15. The test was performed with the same significance levels as above level set for the previous cases. Each of the linear methods provide provides enough pixels within the confident range to isolate the plume pixels. While MF provides the most accurate enhancement values with respect to the nonlinear solver in Fig compared to the GLS (cf. Fig. 14 the SVD better captures the downwind plume, however, peak enhancements are $\approx 30\,\%$ lower. The LLS method does capture the downwind plume but is much less sensitive to enhancement as it significantly underestimates these.

3.8 Errors and correlations

In general the retrieval's fit quality is assessed with respect to the discrepancy between the measurement $\boldsymbol{y}$ and the converged modeled spectrum $\boldsymbol{I}$ according to $\sigma = ||\boldsymbol{y} - \boldsymbol{I}(\hat{\boldsymbol{x}})||$, also known as the residual norm. In order to get the uncertainties (variance) in the estimates of the model parameters for a particular fit, the residual norm is multiplied by the retrieval error covariance matrix

$$\boldsymbol{V} = \frac{\sigma^2}{M - N}(\mathsf{J}^{\mathrm{T}}\,\mathsf{J})^{-1} \quad \text{with} \quad \hat{\boldsymbol{x}}_i \pm \sqrt{\boldsymbol{V_{ii}}}\,, \tag{19}$$

representing the standard error for the fitted state vector $\hat{\boldsymbol{x}}$ and J the Jacobi Jacobian matrix.
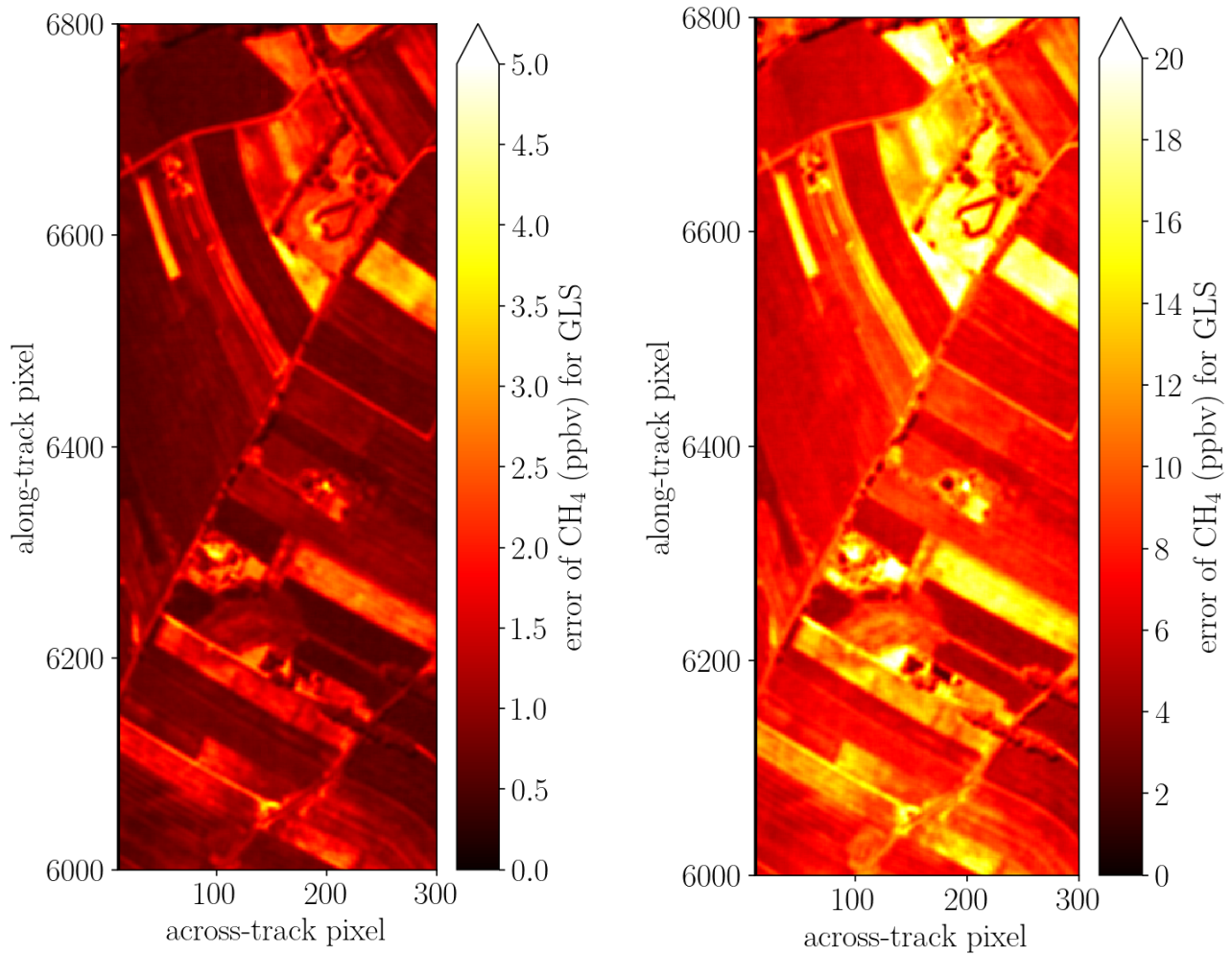
Figure 16. Uncertainties in the estimated CH$_4$ according to Eq. ~~19~~ (19) for the covariance weighted fit in the **(a) (Left)** 4K and **(b) (Right)** 6K spectral windows. The 6K range shows larger errors as it contains less than half the number of pixels than the 4K window. Beside the higher variances also the bad pixel close to methane lines depicted in Fig. 2 is also likely to increase the spectral residuum norm.

The errors of the individual state vector parameters are represented in the square root of the diagonal elements of $\boldsymbol{V}$. The standard error $\sqrt{V_{11}}$ for the CH$_4$ scaling factor is shown ~~inf~~ in Fig. 16. The uncertainty varies with different surface types which is a product of errors induced by correlation and the spectral residual. according to Eq. (19). A different way to evaluate the quality of the retrieval for

440   a scene is to estimate the fit error from the variability of pixels identified as background by the t-test. This method calculates a score by comparing the means of pixels from the target area and the background area, and dividing this by the standard deviation of the background. These values are also obtainable for all the linear fit variants.

Table 2. Mean and standard error for the background pixels of the t-test. Relating the standard error to the mean is a good indication on the accuracy and precision of a method.

| Nonlinear Solvers | Window | Score | Background pixels | |
			mean	std. dev.
GLS	4K	5.34	1832	± 150
GLS	6K	4.94	2051	± 122
GLS	4K6K	4.57	1926	± 170
SLS	4K	3.05	3278	± 673
SLS	6K	2.22	1320	± 537
SLS	4K6K	2.94	3085	± 577
NLS	4K	3.05	3247	± 251
NLS	6K	2.21	1369	± 199
NLS	4K6K	3.40	2840	± 244

Tables 2 and 3 present the findings of this analysis for the nonlinear and linear solvers, respectively. The analysis shows that the GLS fit performs best and that SLS and NLS yield similar results while the MF scores highest amongst the linear solvers. In accordance with Fig. 16 fits in the the 4K window score higher, compared to the 6K. Note that the The less sensitive the retrieval is to CH_4 enhancements the less variations will be observed in the background. Therefore, the standard deviation in the last column should not be overemphasized in the evaluation of the setups.

Table 3. Same as Table 2 but for the linear retrieval setups.

| Linear Solvers | Window | Score | Background pixels | |
			mean	std. dev.
MF	4K	4.22	1778	± 208
MF	6K	3.20	1775	± 217
SVD	4K	3.23	2237	± 383
SVD	6K	3.18	1700	± 157
SLLS	4K	2.72	2069	± 140
SLLS	6K	2.71	1713	± 145

Figure 17 shows the correlation matrix of the retrieval outputs for the various different solvers and spectral intervals. It reveals that most solvers have rather good correlations with the GLS solvers solver (sort of benchmark), particularly in the 4K and multi-window 4K6K spectral ranges. Moreover, the GLS, MF and SVD show blocks of high correlation. Blue colors indicate that

inferred concentrations tend to move in opposite directions which is the case for example in the single window NLS fits shown in Fig. 6.
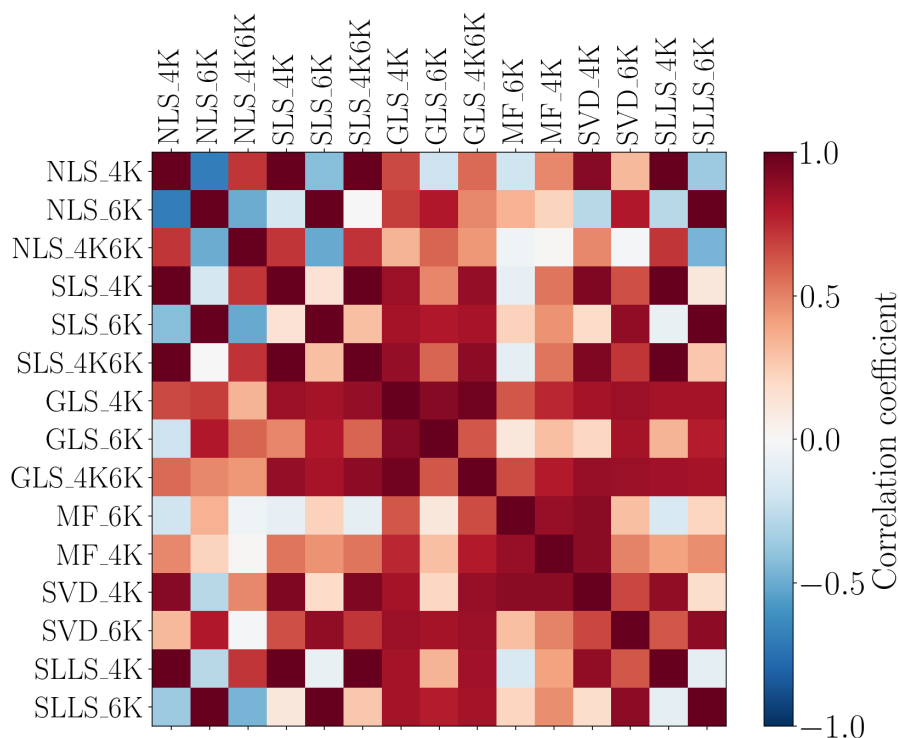
Figure 17. Pearson correlation coefficients for inferred methane from scene 09 for the nonlinear and linear solvers in the two examined spectral intervals.

4 DiscussionsDiscussion

This study found that the BIRRA based nonlinear methods nonlinear setups that which utilize background pixel covariance statistics (GLS) are able suited to quantify CH_4 concentrations with good accuracy and precision . On the other hand, the unweighted BIRRA suffers from and might also allow to quantify emissions. The NLS and SLS fits encounter challenges due to degeneracies between the surface reflectivity and the broad band molecular absorption signal . It was found that the separation of linear (reflectivity coefficients) and nonlinear (target) parameters in the SLS fit does not mitigate the problem of correlation between these quantities but only the inclusion of the background covariance significantly reduces surface reflectance depending biases.

at HySpex resolution. In accordance with Guanter et al. (2021) Borchardt et al. (2021); Guanter et al. (2021) surface brightness and homogeneity were found to be important factors in detecting and quantifying methane plumes. The issue of different surface types and their impact on the uncertainty of the enhancement was also addressed by Borchardt et al. (2021). In accordance with our results the authors noted that retrieval noise can vary significantly depending on surface type, and that different retrieval schemes can yield disparate total column values . A given type of surface

can lead to a positive bias in one spectral window while the opposite may be true in another window (see Fig. 9). For example, they found that paved concrete induces a positive bias while barbed goatgrass leads to a underestimation of enhancements and hence the total columns.

In order to scan for potential CH_4 leakages on large datasets with millions of pixels, linear solvers such as the SVD, MF or LLS are more appropriate due to their significantly better speed performance higher speed (Thompson et al., 2015). While the iterative setups require roughly one second per fit the linear methods are two, up to three orders of magnitude faster. In particular the SVD and MF solvers yield enhancements that often agree well with the more sophisticated nonlinear BIRRA method methods, although their sensitivity and accuracy is lower which in some cases and hampers the ability to detect downwind patterns. Although the SVD method does not explicitly incorporate a covariance matrix it is important to note that the singular vectors are generated from assumed background pixels, hence the solver takes background statistics into account and is considered an equivalent alternative to the MF approach. Both methods are sensitive to the selection of the background and has significant impact on the retrieval result can be significantly hampered by the lack of uniformity in background reflectance (Thorpe et al., 2014; Foote et al., 2020).

The simple linearization of the BIRRA forward model lacks background covariance information

The LLS fit ignores background statistics and hence the fit inversion suffers from albedo correlations similar to its nonlinear counterparts (NLS and SLS). Moreover, the fit The fit also significantly underestimates enhancements although it is able to capture parts of the pattern. For the rather simple SSD method polynomials

Polynomials up to second order were able to capture the enhanced methane signal while the in the rather simple SSD method. The selection of an adequate polynomial is depending on the width of the spectral interval and its surface reflectivity. Note that it Moreover, the method is not designed to quantify methane but only for (tactical onboard) detection.

As mentioned by other authors before (e. g. Thompson et al. 2015) linear methods should be regarded as a complement to other more complete retrieval algorithms. While linear methods are well-suited to survey vast datasets and pinpoint potential sources, the iterative BIRRA solvers are adequate to quantify enhanced concentrations at known locations as the slower speed is not of much concern for some thousands of observations allows for the detection of anomalies in the spectral residuum.

Cluster-tuned linear retrieval setups can help to mitigate background clutter and surface reflectivity induced biases (Nesme et al., 2020), however, incorporation of an adequately compiled background covariance matrix into the fitting scheme was found to be more effective. It was also found that allocating especially if large background areas are selected. Predicting the right cluster for the pixel to be retrieved is crucial in order for the method to improve results as otherwise inaccurate background statistics are used for the fit . Nonetheless, cluster-tuning can pixels impacted by the methane plume is crucial for this method in order to improve fit results. Cluster-tuning can moreover be a beneficial preprocessing step as it e. g. allows to potentially allows to reduce the base vectors per cluster in the SVD method since background variability is reduced and so that fewer base vectors are sufficient to model the background spectrum. However, note that in In this case a separate model matrix A needs to be compiled for each cluster.

While linear methods are well-suited to survey vast datasets and pinpoint potential sources, iterative solvers such as BIRRA are adequate to quantify enhanced concentrations at known locations as the slower speed is not of much concern for some thousands of observations.

5 Conclusions

The study examines the feasibility of methane retrievals from hyperspectral imaging observations ~~using~~ for various retrieval methods. It was found that localized CH_4 enhancements close to the ground can be quantified from HySpex airborne observations. The generalized ~~covariance weighted~~ BIRRA retrieval is well-suited for investigating potential methane emissions. The statement is underpinned by the relatively low background variations and distinct CH_4 enhancement pattern in the surface-albedo covariance weighted BIRRA fits in, e. g., Fig. ~~??~~ 8 and Table 2.

The BIRRA NLS and SLS fits were found to be sensitive to spectral variations in the albedo, leading to surface-type dependent biases ~~that were reported in~~ known from previous studies utilizing data from hyperspectral sensors. This effect ~~was~~ is more pronounced for single spectral intervals but less evident when multiple intervals ~~were used for the fit, such as combining 4K and 6K~~ are combined.

The linear estimators proved to be highly efficient and effective for many cases, making them suitable ~~for near real-time processing in the survey~~ of large hyperspectral datasets. The well-established ~~MF method for hyperspectral data~~ SVD and MF method produced results that ~~often~~ agree well with the BIRRA inferred enhancements, however, they are less sensitive. The LLS method turned out to be the least sensitive one. ~~The SVD method yields similar enhancements and is able to capture most parts of the downwind plume with great statistical confidence. While also the LLS method is able to capture some of the enhanced plume pixels, it is much less sensitive .~~ For detection purposes the SSD was found to be a useful tool.

In conclusion, covariance weighted methods are able to quantify methane enhancements ~~om~~ from hyperspectral SWIR observations at high spatial resolution with good accuracy. ~~The weighted nonlinear methods are more precise and are better~~ In particular the GLS solver is suited to capture ~~the downwind plume which is essential for emission estimates~~ enhancements with an accuracy that should allow for emission estimation. Considering the significant speedup and reasonable accuracy of the linear methods MF and SVD, both constitute a ~~valueable~~ valuable tool in examining plumes on vast datasets.

The methods are ~~applicable to other airborne as well as~~ also applicable to space borne sensors ~~and this should be considered as~~ , which will be considered in a next step. ~~As a final note~~ Overall, the new Python version of the BIRRA code used in this study ~~, based on Py4CAtS as its forward model,~~ turned out to be a flexible toolbox for prototyping.

Code availability. Parts of the code are published via the Py4CAtS software suite (see Schreier et al. (2019))

Data availability. On request

Author contributions. Philipp Hochstaffl (PH) developed and implemented the retrieval setups and analysis tools and wrote the manuscript. Franz Schreier (FS) originally designed and developed the software package Py4CAtS and supported the data evaluation. Claas Köhler (CK) conceived the experimental setup and conducted the data acquisition of the airborne measurements. Andreas Baumgartner (AB) performed

the instrument calibration and Level 0-1 processing. CK, AB contributed the experimental setup to the manuscript. Daniele Cerra (DC) gave valuable advice for the cluster-tuning approach and provided spectral unmixing data for the verification of the SVD and MF results. All authors reviewed the manuscript.

Competing interests. The authors declare that they have no conflict of interest.

Acknowledgements. We thank Thomas Trautmann and Peter Haschberger for valuable criticism of the manuscript. Furthermore we thank Konstantin Gerilowski for initiating coorperation with the CoMet campaign and Andreas Fix as the campaign leader for the support and coordination.

References

References

Anderson, G., Clough, S., Kneizys, F., Chetwynd, J., and Shettle, E.: AFGL atmospheric constituent profiles (0 - 120 km), Tech. Rep. TR-86-0110, AFGL, 1986.

Ayasse, A. K., Thorpe, A. K., Roberts, D. A., Funk, C. C., Dennison, P. E., Frankenberg, C., Steffke, A., and Aubrey, A. D.: Evaluating the Effects of Surface Properties on Methane Retrievals Using a Synthetic Airborne Visible/Infrared Imaging Spectrometer next Generation (AVIRIS-NG) Image, Remote Sens., 215, 386–397, https://doi.org/10.1016/j.rse.2018.06.018, 2018.

Baldridge, A. M., Hook, S. J., Grove, C. I., and Rivera, G.: The ASTER Spectral Library Version 2.0, Remote Sensing of Environment, 113, 711–715, https://doi.org/10.1016/j.rse.2008.11.007, 2009.

Baumgartner, A.: Traceable imaging spectrometer calibration and transformation of geometric and spectral pixel properties, Ph.D. thesis, https://doi.org/10.48693/38, 2021.

Baumgartner, A. and Köhler, C. H.: Transformation of point spread functions on an individual pixel scale, Optics Express, 28, 38 682–38 697, https://doi.org/10.1364/oe.409626, tex.date_added: Tue Dec 15 16:52:19 2020, 2020.

Borchardt, J., Gerilowski, K., Krautwurst, S., Bovensmann, H., Thorpe, A. K., Thompson, D. R., Frankenberg, C., Miller, C. E., Duren, R. M., and Burrows, J. P.: Detection and quantification of CH_4 plumes using the WFM-DOAS retrieval on AVIRIS-NG hyperspectral data, Atmos. Meas. Tech., 14, 1267–1291, https://doi.org/10.5194/amt-14-1267-2021, 2021.

Bruce, P., Bruce, A., and Gedeck, P.: Practical Statistics for Data Scientists: 50+ Essential Concepts Using R and Python, O'Reilly Media, 2020.

Buchwitz, M., Rozanov, V., and Burrows, J.: A near-infrared optimized DOAS method for the fast global retrieval of atmospheric CH_4, CO, CO_2, H_2O, and N_2O total column amounts from SCIAMACHY Envisat-1 nadir radiances, J. Geophys. Res., 105, 15 231–15 245, https://doi.org/10.1029/2000JD900191, 2000.

Buchwitz, M., de Beek, R., Bramstedt, K., Noël, S., Bovensmann, H., and Burrows, J. P.: Global carbon monoxide as retrieved from SCIA-MACHY by WFM-DOAS, Atm. Chem. Phys., 4, 1945–1960, https://doi.org/10.5194/acp-4-1945-2004, 2004.

Buchwitz, M., de Beek, R., Noël, S., Burrows, J. P., Bovensmann, H., Bremer, H., Bergamaschi, P., Körner, S., and Heimann, M.: Carbon monoxide, methane and carbon dioxide columns retrieved from SCIAMACHY by WFM-DOAS: year 2003 initial data set, Atm. Chem. Phys., 5, 3313–3329, https://doi.org/10.5194/acp-5-3313-2005, 2005.

Chabrillat, S., Guanter, L., Segl, K., Foerster, S., Fischer, S., Rossner, G., Schickling, A., LaPorta, L., Honold, H.-P., and Storch, T.: The Enmap German Spaceborne Imaging Spectroscopy Mission: Update and Highlights of Recent Preparatory Activities, in: IGARSS 2020 - 2020 IEEE Intern. Geosci. and Remote Sens. Symposium, pp. 3278–3281, https://doi.org/10.1109/IGARSS39084.2020.9324006, 2020.

Cogliati, S., Sarti, F., Chiarantini, L., Cosi, M., Lorusso, R., Lopinto, E., Miglietta, F., Genesio, L., Guanter, L., Damm, A., Pérez-López, S., Scheffler, D., Tagliabue, G., Panigada, C., Rascher, U., Dowling, T. P. F., Giardino, C., and Colombo, R.: The PRISMA Imaging Spectroscopy Mission: Overview and First Performance Analysis, Remote Sensing of Environment, 262, 112 499, https://doi.org/10.1016/j.rse.2021.112499, 2021.

De Leeuw, G., Kinne, S., Léon, J.-F., Pelon, J., Rosenfeld, D., Schaap, M., Veefkind, P. J., Veihelmann, B., Winker, D. M., and Von Hoyningen-Huene, W.: Retrieval of Aerosol Properties, in: The Remote Sensing of Tropospheric Composition from Space, edited by John P. Burrows, U. P. and Borrell, P., Phys. of Earth and Space Environ., pp. 259–313, Springer-Verlag, https://doi.org/10.1007/978-3-642-14791-3_6, 2011.

Delahaye, T., Armante, R., Scott, N., Jacquinet-Husson, N., Chédin, A., Crépeau, L., Crevoisier, C., Douet, V., Perrin, A., Barbe, A., Boudon, V., Campargue, A., Coudert, L., Ebert, V., Flaud, J.-M., Gamache, R., Jacquemart, D., Jolly, A., Kwabia Tchana, F., Kyuberis, A., Li, G., Lyulin, O., Manceron, L., Mikhailenko, S., Moazzen-Ahmadi, N., Müller, H., Naumenko, O., Nikitin, A., Perevalov, V., Richard, C., Starikova, E., Tashkun, S., Tyuterev, V., Vander Auwera, J., Vispoel, B., Yachmenev, A., and Yurchenko, S.: The 2020 edition of the GEISA spectroscopic database, J. Mol. Spectrosc., 380, 111 510, https://doi.org/https://doi.org/10.1016/j.jms.2021.111510, 2021.

Duren, R. M., Thorpe, A. K., Foster, K. T., Rafiq, T., Hopkins, F. M., Yadav, V., Bue, B. D., Thompson, D. R., Conley, S., Colombi, N. K., Frankenberg, C., McCubbin, I. B., Eastwood, M. L., Falk, M., Herner, J. D., Croes, B. E., Green, R. O., and Miller, C. E.: California's Methane Super-Emitters, Nature, 575, 180–184, https://doi.org/10.1038/s41586-019-1720-3, 2019.

Foote, M. D., Dennison, P. E., Thorpe, A. K., Thompson, D. R., Jongaramrungruang, S., Frankenberg, C., and Joshi, S. C.: Fast and Accurate Retrieval of Methane Concentration From Imaging Spectrometer Data Using Sparsity Prior, IEEE Trans. Geosci. Remote Sens., 58, 6480–6492, https://doi.org/10.1109/TGRS.2020.2976888, 2020.

Frankenberg, C., Platt, U., and Wagner, T.: Retrieval of CO from SCIAMACHY onboard ENVISAT: detection of strongly polluted areas and seasonal patterns in global CO abundances, Atm. Chem. Phys., 5, 1639–1644, https://doi.org/10.5194/acp-5-1639-2005, 2005.

Frankenberg, C., Thorpe, A. K., Thompson, D. R., Hulley, G., Kort, E. A., Vance, N., Borchardt, J., Krings, T., Gerilowski, K., Sweeney, C., Conley, S., Bue, B. D., Aubrey, A. D., Hook, S., and Green, R. O.: Airborne Methane Remote Measurements Reveal Heavy-Tail Flux Distribution in Four Corners Region, Proc. Nat. Academy Sciences, 113, 9734–9739, https://doi.org/10.1073/pnas.1605617113, 2016.

Funk, C., Theiler, J., Roberts, D., and Borel, C.: Clustering to improve matched filter detection of weak gas plumes in hyperspectral thermal imagery, IEEE Transactions on Geoscience and Remote Sensing, 39, 1410–1420, https://doi.org/10.1109/36.934073, 2001.

Gerilowski, K., Tretner, A., Krings, T., Buchwitz, M., Bertagnolio, P. P., Belemezov, F., Erzinger, J., Burrows, J. P., and Bovensmann, H.: MAMAP – a new spectrometer system for column-averaged methane and carbon dioxide observations from aircraft: instrument description and performance analysis, Atmos. Meas. Tech., 4, 215–243, https://doi.org/10.5194/amt-4-215-2011, 2011.

Gimeno García, S., Schreier, F., Lichtenberg, G., and Slijkhuis, S.: Near infrared nadir retrieval of vertical column densities: methodology and application to SCIAMACHY, Atmos. Meas. Tech., 4, 2633–2657, https://doi.org/10.5194/amt-4-2633-2011, 2011.

Golub, G. and Pereyra, V.: Separable nonlinear least squares: the variable projection method and its applications, Inverse Problems, 19, R1–R26, https://doi.org/10.1088/0266-5611/19/2/201, 2003.

Green, R. O., Carrere, V., and Conel, J. E.: Measurement of atmospheric water vapor using the Airborne Visible/Infrared Imaging Spectrometer, in: ASPRS Conference on ImageProcessing, pp. 73–76, 1989.

Green, R. O., Eastwood, M. L., Sarture, C. M., Chrien, T. G., Aronsson, M., Chippendale, B. J., Faust, J. A., Pavri, B. E., Chovit, C. J., Solis, M., Olah, M. R., and Williams, O.: Imaging Spectroscopy and the Airborne Visible/Infrared Imaging Spectrometer (AVIRIS), Remote Sensing of Environment, 65, 227–248, https://doi.org/https://doi.org/10.1016/S0034-4257(98)00064-9, 1998.

Guanter, L., Kaufmann, H., Segl, K., Foerster, S., Rogass, C., Chabrillat, S., Kuester, T., Hollstein, A., Rossner, G., Chlebek, C., Straif, C., Fischer, S., Schrader, S., Storch, T., Heiden, U., Mueller, A., Bachmann, M., Mühle, H., Müller, R., Habermeyer, M., Ohndorf, A., Hill, J., Buddenbaum, H., Hostert, P., Van der Linden, S., Leitão, P. J., Rabe, A., Doerffer, R., Krasemann, H., Xi, H., Mauser, W., Hank, T., Locherer, M., Rast, M., Staenz, K., and Sang, B.: The EnMAP Spaceborne Imaging Spectroscopy Mission for Earth Observation, Remote Sens., 7, 8830–8857, https://doi.org/10.3390/rs70708830, 2015.

Guanter, L., Irakulis-Loitxate, I., Gorroño, J., Sánchez-García, E., Cusworth, D. H., Varon, D. J., Cogliati, S., and Colombo, R.: Mapping methane point emissions with the PRISMA spaceborne imaging spectrometer, Remote Sensing of Environment, 265, 112 671, https://doi.org/https://doi.org/10.1016/j.rse.2021.112671, 2021.

Hansen, P., Pereyra, V., and Scherer, G.: Least Squares Data Fitting with Applications, Johns Hopkins University Press, 2013.

Hochstaffl, P. and Schreier, F.: Impact of Molecular Spectroscopy on Carbon Monoxide Abundances from SCIAMACHY, Remote Sens., 12, 1084, https://doi.org/10.3390/rs12071084, 2020.

610 Hochstaffl, P., Schreier, F., Lichtenberg, G., and Gimeno García, S.: Validation of Carbon Monoxide Total Column Retrievals from SCIA-MACHY Observations with NDACC/TCCON Ground-Based Measurements, Remote Sens., 10, 223, https://doi.org/10.3390/rs10020223, 2018.

Hochstaffl, P., Schreier, F., Birk, M., Wagner, G., Feist, G. D., Notholt, J., Sussmann, R., and Té, Y.: Impact of Molecular Spectroscopy on Carbon Monoxide Abundances from TROPOMI, Remote Sens., 12, 3486, https://doi.org/10.3390/rs12213486, 2020.

615 Hochstaffl, P.: Trace Gas Concentration Retrieval from Short-Wave Infrared Nadir Sounding Spaceborne Spectrometers, Ph.D. thesis, Ludwig-Maximilians-Universität München, 2022.

Hochstaffl, P., Baumgartner, A., Slijkhuis, S., Lichtenberg, G., Koehler, C. H., Schreier, F., Roiger, A., Feist, D. G., Marshall, J., Butz, A., and Trautmann, T.: CO2Image Retrieval Studies and Performance Analysis, Tech. Rep. EGU23-15635, Copernicus Meetings, https://doi.org/10.5194/egusphere-egu23-15635, 2023.

620 Humpage, N., Boesch, H., Palmer, P. I., Vick, A., Parr-Burman, P., Wells, M., Pearson, D., Strachan, J., and Bezawada, N.: GreenHouse gas Observations of the Stratosphere and Troposphere (GHOST): an airborne shortwave-infrared spectrometer for remote sensing of greenhouse gases, Atmos. Meas. Tech., 11, 5199–5222, https://doi.org/10.5194/amt-11-5199-2018, 2018.

(IMF), D. R. S. T. I.: Airborne imaging spectrometer HySpex, Journal of large-scale research facilities, 2, 1–6, https://doi.org/10.17815/jlsrf-2-151, 2016.

625 Intergovernmental Panel on Climate Change: Climate Change 2013 – The Physical Science Basis: Working Group I Contribution to the Fifth Assessment Report of the Intergovernmental Panel on Climate Change, Cambridge University Press, https://doi.org/10.1017/CBO9781107415324, 2014.

Jervis, D., McKeever, J., Durak, B. O. A., Sloan, J. J., Gains, D., Varon, D. J., Ramier, A., Strupler, M., and Tarrant, E.: The GHGSat-D imaging spectrometer, Atmos. Meas. Tech., 14, 2127–2140, https://doi.org/10.5194/amt-14-2127-2021, 2021.

630 Kalnay, E., Kanamitsu, M., Kistler, R., Collins, W., Deaven, D., Gandin, L., Iredell, M., Saha, S., White, G., Woollen, J., Zhu, Y., Chelliah, M., Ebisuzaki, W., Higgins, W., Janowiak, J., Mo, K. C., Ropelewski, C., Wang, J., Leetmaa, A., Reynolds, R., Jenne, R., and Joseph, D.: The NCEP/NCAR 40-Year Reanalysis Project, Bull. Am. Met. Soc., 77, 437–472, https://doi.org/10.1175/1520-0477(1996)077<0437:TNYRP>2.0.CO;2, 1996.

C. H.\ Köhler: Airborne Imaging Spectrometer HySpex, J Large-Scale Res Facil. JLSRF, 2, 1–6, 2016.

635 Krings, T., Gerilowski, K., Buchwitz, M., Reuter, M., Tretner, A., Erzinger, J., Heinze, D., Pflüger, U., Burrows, J. P., and Bovensmann, H.: MAMAP — a new spectrometer system for column-averaged methane and carbon dioxide observations from aircraft: retrieval algorithm and first inversions for point source emission rates, Atmos. Meas. Tech., 4, 1735–1758, https://doi.org/10.5194/amt-4-1735-2011, 2011.

Kuze, A., Suto, H., Nakajima, M., and Hamazaki, T.: Thermal and near infrared sensor for carbon observation Fourier-transform spectrometer on the Greenhouse Gases Observing Satellite for greenhouse gases monitoring, Appl. Opt., 48, 6716–6733,
640 https://doi.org/10.1364/AO.48.006716, 2009.

Kuze, A., Suto, H., Shiomi, K., Kawakami, S., Tanaka, M., Ueda, Y., Deguchi, A., Yoshida, J., Yamamoto, Y., Kataoka, F., Taylor, T. E., and Buijs, H. L.: Update on GOSAT TANSO-FTS performance, operations, and data products after more than 6 years in space, Atmos. Meas. Tech., 9, 2445–2461, https://doi.org/10.5194/amt-9-2445-2016, 2016.

Lauvaux, T., Giron, C., Mazzolini, M., d'Aspremont, A., Duren, R., Cusworth, D., Shindell, D., and Ciais, P.: Global assessment of oil and gas methane ultra-emitters, Science, 375, 557–561, https://doi.org/10.1126/science.abj4351, 2022.

Lenhard, K., Baumgartner, A., and Schwarzmaier, T.: Independent laboratory characterization of neo HySpex imaging spectrometers VNIR-1600 and SWIR-320Gm-e, IEEE Transactions on Geoscience and Remote Sensing, 53, 1828–1841, https://doi.org/10.1109/tgrs.2014.2349737, tex.date_added: Fri May 24 16:15:14 2019, 2015.

Liou, K.-N.: An Introduction to Atmospheric Radiation, Academic Press, second edn., 2002.

Lorente, A., Borsdorff, T., Butz, A., Hasekamp, O., aan de Brugh, J., Schneider, A., Wu, L., Hase, F., Kivi, R., Wunch, D., Pollard, D. F., Shiomi, K., Deutscher, N. M., Velazco, V. A., Roehl, C. M., Wennberg, P. O., Warneke, T., and Landgraf, J.: Methane retrieved from TROPOMI: improvement of the data product and validation of the first 2 years of measurements, Atmos. Meas. Tech., 14, 665–684, https://doi.org/10.5194/amt-14-665-2021, 2021.

Luther, A., Kleinschek, R., Scheidweiler, L., Defratyka, S., Stanisavljevic, M., Forstmaier, A., Dandocsi, A., Wolff, S., Dubravica, D., Wildmann, N., Kostinek, J., Jöckel, P., Nickl, A.-L., Klausner, T., Hase, F., Frey, M., Chen, J., Dietrich, F., Necki, J., Swolkień, J., Fix, A., Roiger, A., and Butz, A.: Towards verifying CH_4 emissions from hard coal mines using mobile sun-viewing Fourier transform spectrometry, Atmos. Meas. Tech. Disc., 2019, 1–19, https://doi.org/10.5194/amt-2019-205, 2019.

Luther, A., Kostinek, J., Kleinschek, R., Defratyka, S., Stanisavljević, M., Forstmaier, A., Dandocsi, A., Scheidweiler, L., Dubravica, D., Wildmann, N., Hase, F., Frey, M. M., Chen, J., Dietrich, F., Necki, J., Swolkień, J., Knote, C., Vardag, S. N., Roiger, A., and Butz, A.: Observational constraints on methane emissions from Polish coal mines using a ground-based remote sensing network, Atmospheric Chemistry and Physics, 22, 5859–5876, https://doi.org/10.5194/acp-22-5859-2022, publisher: Copernicus GmbH, 2022.

Masson-Delmotte, V., Zhai, P., Pirani, A., Connors, S., Péan, C., Berger, S., Caud, N., Chen, Y., Goldfarb, L., Gomis, M., Huang, M., Leitzell, K., Lonnoy, E., Matthews, J., Maycock, T., Waterfield, T., Yelekçi, O., Yu, R., and (eds.), B. Z.: Climate Change 2021: The Physical Science Basis. Contribution of Working Group I to the Sixth Assessment Report of the Intergovernmental Panel on Climate Change, Cambridge University Press, https://doi.org/10.1017/CBO9781107415324, 2021.

Meerdink, S. K., Hook, S. J., Roberts, D. A., and Abbott, E. A.: The ECOSTRESS Spectral Library Version 1.0, Remote Sensing of Environment, 230, 111 196, https://doi.org/10.1016/j.rse.2019.05.015, 2019.

Nesme, N., Foucher, P.-Y., and Doz, S.: Detection and quantification of industrial methane plume with the airborne Hyspex-NEO camera and applications to satellite data, in: XXIV ISPRS Congress 2020 edition, vol. XLIII-B3-2020, pp. 821 – 827, Online, France, https://doi.org/10.5194/isprs-archives-xliii-b3-2020-821-2020, 2020.

Nickl, A.-L., Mertens, M., Roiger, A., Fix, A., Amediek, A., Fiehn, A., Gerbig, C., Galkowski, M., Kerkweg, A., Klausner, T., Eckl, M., and Jöckel, P.: Hindcasting and forecasting of regional methane from coal mine emissions in the Upper Silesian Coal Basin using the online nested global regional chemistry–climate model MECO(n) (MESSy v2.53), Geoscientific Model Development, 13, 1925–1943, https://doi.org/10.5194/gmd-13-1925-2020, 2020.

OpenStreetMap contributors: Planet dump retrieved from https://planet.osm.org, https://www.openstreetmap.org, 2022.

Pandya, M. R., Chhabra, A., Pathak, V. N., Trivedi, H., and Chauhan, P.: Mapping of thermal power plant emitted atmospheric carbon dioxide concentration using AVIRIS-NG data and atmospheric radiative transfer model simulations, J. Appl. Remote Sens., 15, https://doi.org/10.1117/1.jrs.15.032204, 2021.

Rast, M., Nieke, J., Adams, J., Isola, C., and Gascon, F.: Copernicus Hyperspectral Imaging Mission for the Environment (Chime), in: 2021 IEEE International Geoscience and Remote Sensing Symposium IGARSS, pp. 108–111, https://doi.org/10.1109/IGARSS47720.2021.9553319, 2021.

Richter, A.: Satellite remote sensing of tropospheric composition - principles, results, and challenges, EPJ Web of Conferences, 9, 181–189, https://doi.org/10.1051/epjconf/201009014, 2010.

Schneising, O., Buchwitz, M., Burrows, J. P., Bovensmann, H., Bergamaschi, P., and Peters, W.: Three years of greenhouse gas column-averaged dry air mole fractions retrieved from satellite — Part 2: Methane, Atm. Chem. Phys., 9, 443–465, https://doi.org/10.5194/acp-9-443-2009, 2009.

Schreier, F., Gimeno García, S., Milz, M., Kottayil, A., Höpfner, M., von Clarmann, T., and Stiller, G.: Intercomparison of Three Microwave/Infrared High Resolution Line-by-Line Radiative Transfer Codes, in: Radiation Processes in the Atmosphere and Ocean (IRS2012): Proceedings of the International Radiation Symposium (IRC/IAMAS), edited by Cahalan, R. F. and Fischer, J., vol. 1531 of *AIP Conference Proceedings*, pp. 119–122, https://doi.org/10.1063/1.4804722, 2013.

Schreier, F., Gimeno García, S., Hedelt, P., Hess, M., Mendrok, J., Vasquez, M., and Xu, J.: GARLIC – A General Purpose Atmospheric Radiative Transfer Line-by-Line Infrared-Microwave Code: Implementation and Evaluation, J. Quant. Spectrosc. & Radiat. Transfer, 137, 29–50, https://doi.org/10.1016/j.jqsrt.2013.11.018, 2014.

Schreier, F., Gimeno García, S., Hochstaffl, P., and Städt, S.: Py4CAtS — PYthon for Computational ATmospheric Spectroscopy, Atmosphere, 10, 262, https://doi.org/10.3390/atmos10050262, 2019.

Theiler, J. and Foy, B.: Effect of signal contamination in matched-filter detection of the signal on a cluttered background, Geosci. Remote Sens. Letters, 3, 98–102, https://doi.org/10.1109/LGRS.2005.857619, 2006.

Thompson, D. R., Leifer, I., Bovensmann, H., Eastwood, M., Fladeland, M., Frankenberg, C., Gerilowski, K., Green, R. O., Kratwurst, S., Krings, T., Luna, B., and Thorpe, A. K.: Real-time remote detection and measurement for airborne imaging spectroscopy: a case study with methane, Atmos. Meas. Tech., 8, 4383–4397, https://doi.org/10.5194/amt-8-4383-2015, 2015.

Thompson, D. R., Thorpe, A. K., Frankenberg, C., Green, R. O., Duren, R., Guanter, L., Hollstein, A., Middleton, E., Ong, L., and Ungar, S.: Space-based remote imaging spectroscopy of the Aliso Canyon CH4 superemitter, Geophys. Res. Letters, 43, 6571–6578, https://doi.org/https://doi.org/10.1002/2016GL069079, 2016.

Thorndike, R. L.: Who belongs in the family, Psychometrika, pp. 267–276, 1953.

Thorpe, A. K., Roberts, D. A., Bradley, E. S., Funk, C. C., Dennison, P. E., and Leifer, I.: High resolution mapping of methane emissions from marine and terrestrial sources using a Cluster-Tuned Matched Filter technique and imaging spectrometry, Remote Sensing of Environment, 134, 305–318, https://doi.org/https://doi.org/10.1016/j.rse.2013.03.018, 2013.

Thorpe, A. K., Frankenberg, C., and Roberts, D. A.: Retrieval techniques for airborne imaging of methane concentrations using high spatial and moderate spectral resolution: application to AVIRIS, Atmos. Meas. Tech., 7, 491–506, https://doi.org/10.5194/amt-7-491-2014, 2014.

United Nations Framework Convention on Climate: Paris Agreement to the United Nations Framework Convention on Climate Change, https://unfccc.int/files/meetings/paris_nov_2015/application/pdf/paris_agreement_english_.pdf, accessed: 2021-04-01, 2015.

Varon, D. J., Jacob, D. J., McKeever, J., Jervis, D., Durak, B. O. A., Xia, Y., and Huang, Y.: Quantifying Methane Point Sources from Fine-Scale Satellite Observations of Atmospheric Methane Plumes, Atmos. Meas. Tech., 11, 5673–5686, https://doi.org/10.5194/amt-11-5673-2018, 2018.

Varon, D. J., McKeever, J., Jervis, D., Maasakkers, J. D., Pandey, S., Houweling, S., Aben, I., Scarpelli, T., and Jacob, D. J.: Satellite Discovery of Anomalously Large Methane Point Sources From Oil/Gas Production, Geophys. Res. Letters, 46, 13 507–13 516, https://doi.org/https://doi.org/10.1029/2019GL083798, 2019.

Veefkind, J., Aben, I., McMullan, K., Förster, H., de Vries, J., Otter, G., Claas, J., Eskes, H., de Haan, J., Kleipool, Q., van Weele, M., Hasekamp, O., Hoogeveen, R., Landgraf, J., Snel, R., Tol, P., Ingmann, P., Voors, R., Kruizinga, B., Vink, R., Visser, H., and Levelt,

720   P.: TROPOMI on the ESA Sentinel-5 Precursor: A GMES mission for global observations of the atmospheric composition for climate, air quality and ozone layer applications, Remote Sensing of Environment, 120, 70 – 83, https://doi.org/10.1016/j.rse.2011.09.027, the Sentinel Missions - New Opportunities for Science, 2012.

Villeneuve, P. V., Fry, H. A., Theiler, J. P., Clodius, W. B., Smith, B. W., and Stocker, A. D.: Improved matched-filter detection techniques, in: Imaging Spectrometry V, edited by Descour, M. R. and Shen, S. S., vol. 3753, pp. 278 – 285, International Society for Optics and

725   Photonics, Proc. SPIE, https://doi.org/10.1117/12.366290, 1999.

Zdunkowski, W., Trautmann, T., and Bott, A.: Radiation in the Atmosphere: A Course in Theoretical Meteorology, Cambridge University Press, 2007.